FACULTY
OF MATHEMATICS
AND PHYSICS
Charles University

MASTER'S THESIS

Jakub Jungwirth

Application of chiroptical techniques for exploration of inhomogeneous systems

Department of Chemical Physics and Optics

Supervisor of the master's thesis: Prof. RNDr. Petr Bouř, CSc.

Study programme: Physics

Study branch: Optics and Optoelectronics

Prague 2017

I declare that I carried out this master's thesis independently, and only with the cited sources, literature and other professional sources.

I understand that my work relates to the rights and obligations under the Act No. 121/2000 Sb., the Copyright Act, as amended, in particular the fact that the Charles University has the right to conclude a license agreement on the use of this work as a school work pursuant to Section 60 subsection 1 of the Copyright Act.

In Prague 12. 5. 2017   _____

Title: Application of chiroptical techniques for exploration of inhomogeneous systems

Author: Jakub Jungwirth

Department: Department of Chemical Physics and Optics

Supervisor: Prof. RNDr. Petr Bouř, CSc.,
Institute of Organic Chemistry and Biochemistry, Czech Academy of Sciences

Abstract: Understanding molecular structure of biochemically relevant molecules is of fundamental interest for these molecules ultimately determine all functions of living organisms. Raman optical activity (ROA) is a chiroptical spectroscopic technique highly sensitive to molecular structure. This thesis presents an introduction to important concepts of ROA and two independent projects aiming to extend the possibilities of ROA, both from theoretical and experimental points of view. The first project is a conformational analysis of dialanine, an important model peptide. A combined quantum mechanics / molecular dynamics approach was used in spectral simulations and resulted in spectra with an unprecedented agreement with experiment. To obtain information about conformer equilibria, a decomposition procedure of an experimental spectrum into calculated individual conformer spectra was coded and tested, and proved to be a viable approach. The second project was an attempt to carry out pioneering ROA measurements of amyloid fibrils, which are difficult to measure due to their inhomogeneous nature (insolubility, birefringence). Within this project, the preparation protocol for such samples was improved. The performance of an all new rotational cuvette was examined and found to suffer from fluorescence problems. Also, ROA measurement in various polarization modes was tested, preliminary results suggest the SCP mode to be least prone to false signals. Although some progress was made, the ultimate goal of obtaining faithful, reproducible ROA spectra of amyloid fibrils has not been achieved.

(Master's Thesis Assignment in Czech)

UNIVERZITA KARLOVA V PRAZE
Matematicko-fyzikální fakulta

Katedra chemické fyziky a optiky   Akademický rok: 2016/2017

ZADÁNÍ DIPLOMOVÉ PRÁCE

Jméno a příjmení: **Jakub Jungwirth**

Studijní program: **Fyzika**

Studijní obor: **Optika a optoelektronika**

Děkan fakulty Vám podle zákona č. 111/1998 Sb. určuje tuto diplomovou práci:

Název práce: **Application of chiroptical techniques for exploration of inhomogeneous systems**

Anglický název práce: **Application of chiroptical techniques for exploration of inhomogeneous systems**

Zásady pro vypracování:

Chirální spektroskopické techniky (cirkulární dichroismus, Ramanova optická aktivita) jsou výjimečně citlivé k molekulární struktuře. Současně však může být měření snadno znehodnoceno falešnými signály, zejména u nehomogenních vzorků. Jejich měření je například žádoucí pro pochopení struktury proteinových agregátů doprovázející některé neurodegenerativní choroby. Cílem práce navrhnout úpravy spektrometru pro optimalizované měření spekter z rozptylujících vzorků a za pomoci teoretického modelování pochopit vztah mezi strukturou a spektrem modelových látek.
V experimentální části práce bude ROA spektrometr měřící kruhově polarizovanou složku v rozptýleném záření (SCP) rozšířen i pro měření ostatních modulačních schémat (ICP a DCPI a DCPII,). Jedno z možných řešení (viz. např. Nafie, JRS 2012, 43, 89–94) je možné provést tak, že optická sestava ROA spektrometru bude doplněna o fázovou lambda/4 desku (otáčenou o úhel +/- 45° pro generaci LCP a RCP záření) a lambda/2 desku, která se bude zasouvat do optické dráhy excitačního záření, přičemž jednotlivé mechanické pohyby musí být sfázovány s měřícím cyklem ROA spektrometru.

Předběžný plán
1. Srovnání ICP a SCP ROA experimentu při měření nehomogenních vzorků (práškové vzorky, nehomogenní roztok/sraženina/fibrily peptidů a proteinů).
2. Simulace vibrační optické aktivity modelového peptidu (Ala-Ala) zahrnující anharmonické a solvatační efekty.
3. Simulace vibrační optické aktivity modelových proteinů (Alan, AK25, poly(L-Glu), poly(L-Lys) apod).
4. Případné srovnání VCD a ROA spekter fibrilárních proteinů

Seznam odborné literatury:

Literatura:
Barron, L. D.: Molecular Light Scattering and Optical Activity, Cambridge, University Press, 2004
Nafie, L.: Vibrational optical activity: Principles and applications, Chichester, Wiley, 2011
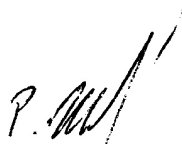
v

Vedoucí diplomové práce: **doc. RNDr. Bouř Petr, CSc.**

Navrhovaní oponenti:
Konzultanti:
Datum zadání diplomové práce: 25.11.2015

Termín odevzdání diplomové práce: dle harmonogramu příslušného akademického roku

....
Vedoucí katedry

....
Děkan

V Praze dne 16.3.2016

Dedicated to the handful of readers.

Without them, none of this would have been possible.

x

Contents

Preface

Biochemical molecules may be regarded as the ultimate clockwork determining all functions of living organisms. Chiroptical spectroscopic techniques are an exceptional tool for observing what is happening in this intriguing nanoscale world. The aim of this thesis is to expand the capabilities one such technique, Raman optical activity. This is attempted both from theoretical and experimental points of view.

Following an introduction, two chapters (2 and 3) are dedicated to explaining experimental and theoretical aspects of Raman optical activity. Chapter 4 presents a conformational study of the dialanine dipeptide based on experimental spectra simulations from first principles. Chapter 5 is purely experimental in character. It presents the progress made in attempts to acquire spectra of amyloid fibrils, which form inhomogeneous samples. Since both presented projects were not done solitarily by the author but rather as part of a team effort, a section at the end of each relevant chapter is added declaring authorship of the work.

As the thesis crosses borders of scientific fields (physics, chemistry) and academic institutions (Charles University, Institute of Organic Chemistry and Biochemistry, Palacký University), it was not obvious to which audience the text should be oriented. The choice was made to mainly suit readers from where the thesis is to be presented; Charles University, Faculty of Mathematics and Physics, School of Physics. It is thus anticipated that the reader possesses a basic understanding of electromagnetism, optics, quantum mechanics and thermodynamics. On the other hand, more effort was made to explain underlying biochemical concepts.

The author would like to acknowledge all coworkers for their contributions. The number them is too high to be listed here, most of them are mentioned at the end of corresponding chapters. One explicit acknowledgement needs to be stated here, however. That is to the thesis supervisor Petr Bouř for always finding time to explain or discuss intricacies encountered in the course of research, and also for providing many valuable comments to the preparation of this manuscript.

1. Introduction

The term optical activity encompasses a large family of phenomena connected by the difference in response of matter to right- and left-circularly polarized light. Pioneering work in this field was that of Fresnel and Pasteur, who realized the intimate connection between optical rotation and chirality of a substance. Tremendously important was Faraday's demonstration of optical rotation induced by a magnetic field, which demonstrated the connection between electromagnetism and light.

Historically, optical activity has been associated mostly with electronic transitions in matter. The dramatic advancements in optical and electronic technology in the 1960s and following decades (invention of the laser, electro-optic modulator — Pockels cell and charge-coupled device; just to name a few) allowed for optical activity measurements in the vibrational region. This new field of spectroscopy termed vibrational optical activity greatly expanded the amount of information that can be obtained about molecular structure. Infrared and Raman techniques both provide important, often complementary information.

The infrared technique of vibrational circular dichroism (VCD) would be defined as the difference in absorbance between left and right circularly polarized light for a molecule undergoing a vibrational transition [Nafie, 2011]. Vibrational Raman optical activity (ROA) is defined as the difference in Raman scattering intensity between right- and left-circularly polarized incident and/or scattered radiation [Nafie, 2011]. Schematically this is illustrated in figure 1.1.
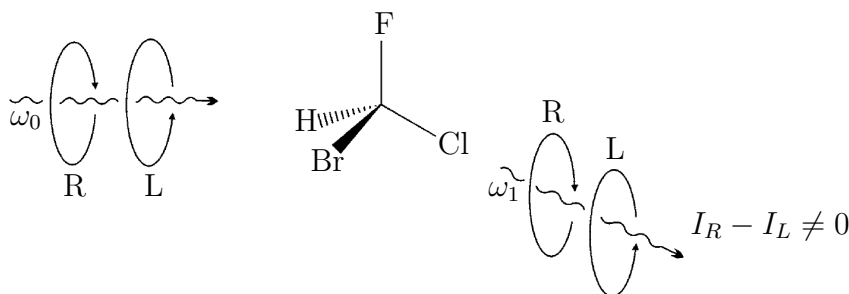

Figure 1.1: Schematic representation of an ROA measurement. Upon Raman scattering from a chiral molecule, intensities of right- and left-circularly polarized scattered light (I_R, I_L) are not equal. ω_0 and ω_1 are incident and scattered frequencies. Adapted from [Barron, 2015].

A typical area of vibrational optical activity application would be the realm of biomolecules, where chirality is omnipresent. Importantly, ROA allows for chemical structure studies of molecules in their natural environment — in water solution. For biologically relevant molecules, other structural methods often come short. A problem with X-ray crystallography is that not all peptides, proteins etc. crystallize and even for those that do, some doubt about the equivalence of solution and crystal structure remains. Nuclear magnetic resonance (NMR) usually cannot resolve systems containing more than a few hundred atoms, and absolute configuration can be obtained from NMR only through an interaction with another system (solvent or reagent) of known chirality [Seco et al., 2004].

ROA spectra are often more informative than "parent" Raman spectra, i.e. those where circular components of light are added rather than subtracted. The largest ROA signals come from the most rigid and chiral parts of the molecules. In polypeptides, for example, the ROA spectrum is dominated by signals from the backbone, whereas Raman spectra of these species are usually dominated by amino acid side chains, thus obscuring the backbone structure information. [Barron, 2004], [Barron, 2015]

Optical activity can either be induced by an external magnetic field. We speak of natural optical activity if the substance is optically active in the absence of external fields. In the latter case the reason for the different response to right- and left-circularly polarized light is chirality (from the Greek word χειρ – kheir, meaning hand). This means the mirror image of the sample cannot be brought to coincide with itself, just like the right and left hands.

1.1   The Biochemical Minimum

In this section, basic concepts needed to understand the biochemical implications of the remainder of the thesis will be explained. These are mainly associated with protein sturcture. Readers with basic training in biochemistry, please feel free to skip to page 9. Otherwise you are asked to forgive the author for some simplifications.

Biomolecule. Generally any molecule naturally present in living organisms and not abundantly found elsewhere (e.g. H_2O would not be considered a biomolecule). Most biomolecules are made of primarily the elements carbon, hydrogen, oxygen and nitrogen, sulfur and phosphorus are also frequently found. Important classes are carbohydrates (sugars), lipids (fats), proteins and nucleic acids (DNA).

Polar and non-polar molecules. Biomolecules can be classified as polar or non-polar depending on whether their electronic charge distribution varies significantly across the molecule or is rather uniform, respectively. Non-polar biomolecules are dominantly composed of carbon and hydrogen (e.g. lipids), whereas for polar molecules a high oxygen content is typical. Charge distribution determines how well two substances mix, polar mix well with polar, non-polar mix well with non-polar, but for example fat and water do not.

Covalent and non-covalent bonding. Roughly speaking, a covalent chemical bond results from an energetically favorable electronic orbital overlap between neighboring atoms. Non-covalent bonding is primarily the result of electrostatic attraction. Covalent bonds are typically stronger. Non-covalent bonds may occur both between different molecules or be intramolecular.

An important example of non-covalent bonding are hydrogen bonds. In an O–H or N–H bond, a lower electron density is present near the hydrogen, so it possesses a partial positive charge and can be bound to groups with higher electron densities. This is illustrated in figure 1.2. The length of hydrogen bonds in water is often considered to be 197 pm.
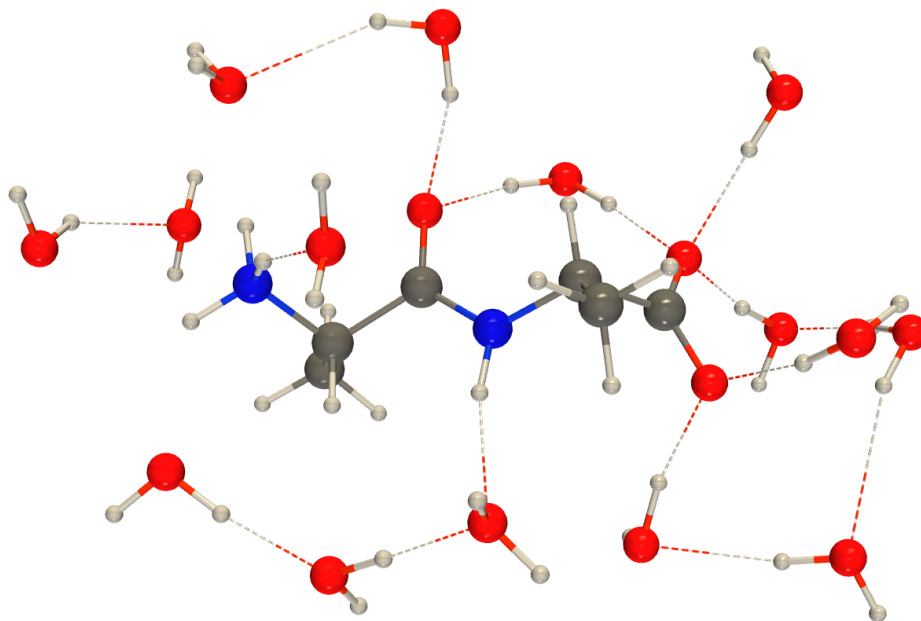
Figure 1.2: L-alanyl-L-alanine surrounded by a cluster of water molecules. Full lines represent covalent bonds, dotted lines are hydrogen bonds. Even though the existence of a particular hydrogen bond in this example is very temporary (at ambient temperature), their general existence decreases intramolecular non-covalent interactions which leads to profound changes in molecular structure of L-alanyl-L-alanine. Standard coloring is used for the atoms (C, H, O, N).

Amino acids, peptides, proteins. Among other things, amino acids are important building blocks of larger biomolecules. Their chemical constitution can be found depicted on the left hand side of figure 1.3 (page 8), where R represents a group of atoms ranging in size from one to eighteen atoms. As can be seen in figure 1.3, two amino acids may react with each other resulting in a molecule that, again, possesses an amino group ($-NH_3^+$) on one end and a carboxylic acid group ($-COO^-$) on the other. Therefore the product may undertake a similar reaction over and over again. When $2 - 100$ amino acids assemble by forming an amide bond[1], the resulting molecule is referred to as a peptide, when this number exceeds 100 we speak of proteins. The ends of such molecules are referred to as the N- and C-terminus respectively.

Electroneutral and zwitterionic species. Looking at figure 1.3 once more, one might ask why the N-terminus is positively charged and the C-terminus negatively charged, when electroneutral forms of both groups ($-NH_2$ and $-COOH$) commonly exist. Amino acids would adopt the electroneutral forms of their termini in the gas phase, for example, but when solvated in water, transfer of the hydrogen leads to energetically favorable electrostatic interactions with the solvent (hydrogen bonding). Amino acids adopt the
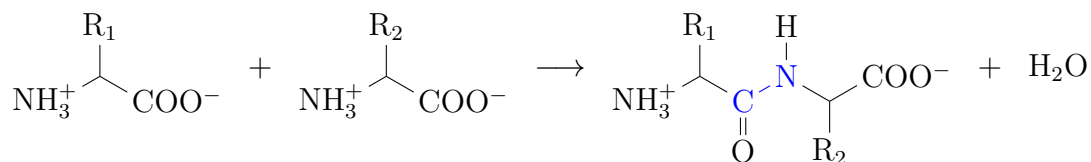
---

[1]Often also termed peptide bond.

Figure 1.3: A chemical reaction of two amino acids resulting in the formation of an amide bond (blue), and water. $R_{1/2}$ is one of twenty possible groups coded in DNA ranging in size from 1 to 18 atoms.

zwitterionic form at their isoelectric point (a characteristic value of pH), more acidic pH results in protonation (addition of hydrogen) to the C-terminus resulting in an overall positively charged molecule, and similarly moving to more basic pH results in deprotonation of the N-terminus. The term zwitterion is derived from the German word zwitter meaning hermaphrodite.

Primary, secondary and tertiary protein structure. When discussing peptide and protein structure, multiple levels of organization are distinguished. So called primary structure is simply the list of amino acids forming the chain ordered from the N- to the C-terminus. Intramolecular non-covalent bonds (most importatly hydrogen bonds) lead to stabilization of the peptide chain, which results in relatively fixed so called secondary structures. Two important examples are depicted in figure 1.4. A single secondary structure usually does not persist throughout an entire protein. The spatial organization of various segments of a defined secondary structure is referred to as protein tertiary structure.

Peptide backbone torsional angles and Ramachandran plots. Torsional (dihedral) angles of the peptide backbone are commonly used to discuss peptide secondary structure. Definition of the ψ, ω and φ angles is depicted in figure 1.5. Since ω rarely deviates from values near 180°, it is usually
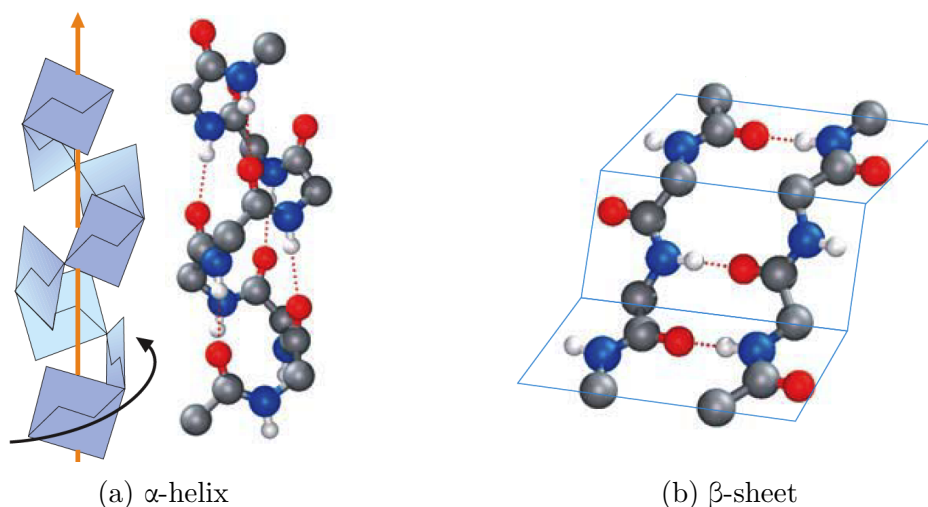

(a) α-helix

(b) β-sheet

Figure 1.4: Two peptide/protein secondary structures stabilized by hydrogen bonds (dotted lines). From [Koolman et al., 2005].

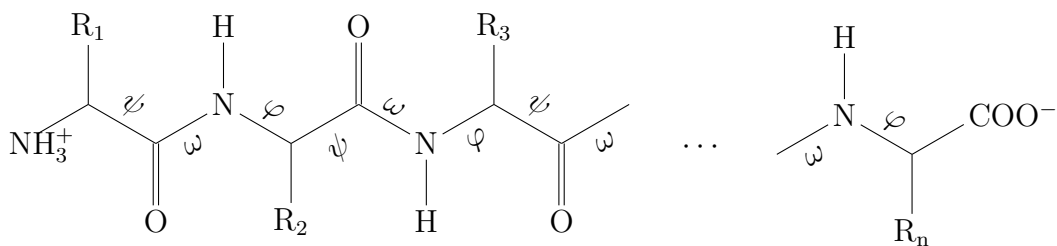Figure 1.5: Peptide backbone torsional angles ψ, ω, φ. The four atoms needed to define a dihedral angle are always chosen along the backbone.

sufficient to consider only ψ and φ. For example, the values $\varphi = -57°$ and $\psi = -47°$ are characteristic for α-helices. Ramachandran plots are visualizations of conformational energies as a function of the φ and ψ angles, one such plot is given in figure 4.6 (page 33).

Enantiomer. The mirror image of a chiral molecule. Also known as optical isomer because all optical activity measurements give the same result with opposite sign.[2] Commonly used labels to distinguish enantiomers are $+/-$, R/S or D/L.

Absolute configuration. Specification of a specific enantiomer. Absolute configuration is critical for biological activity and toxicity of compounds.

1.2 Overview of ROA Development and Contemporary Areas of Application

As could be expected, ROA did not emerge overnight. Ideas about its existence [Kastler, 1930] appeared very soon after the dawn of quantum theory and the discovery of the Raman effect, but a molecular theory of ROA spotted the light of day decades later [Atkins and Barron, 1969, Barron and Buckingham, 1971]. First experimental observations on simple organic molecules soon followed [Barron et al., 1973, Hug et al., 1975], see figure 1.6 (page 10).

It took another 15 years of experimental instrumentation development for an ROA signal of biomolecules to be measured, such as trans-pinane and alanine [Hecht et al., 1989]. A milestone for the spread of ROA measurement to a wider community was the introduction of a commercial instrument by BioTools, Inc. in 2003 based on a design of Hug and Hangartner [1999].

The majority of measurements presented in this thesis were performed using this instrument — the BioTools ChiralRAMAN-2X™. To give a personal view about it, it is not exactly what you would call a *black box* instrument. One still has access to all of the optical components, which can be (and often need to be) cleaned, aligned or modified. Also samples requiring special handling need nonstandard cells to be measured in, for example a temperature controlled

---

[2]Strictly speaking, an optical isomer would be a mirror image composed of antimatter as a consequence of CP (charge, parity) symmetry [Barron, 2004]. However interesting that might be, bare in mind that the difference of an ROA signal between matter and antimatter is by no means detectable. Nor can this claim be tested because the timescales of ROA acquisition and antimatter confinement do not really meet.
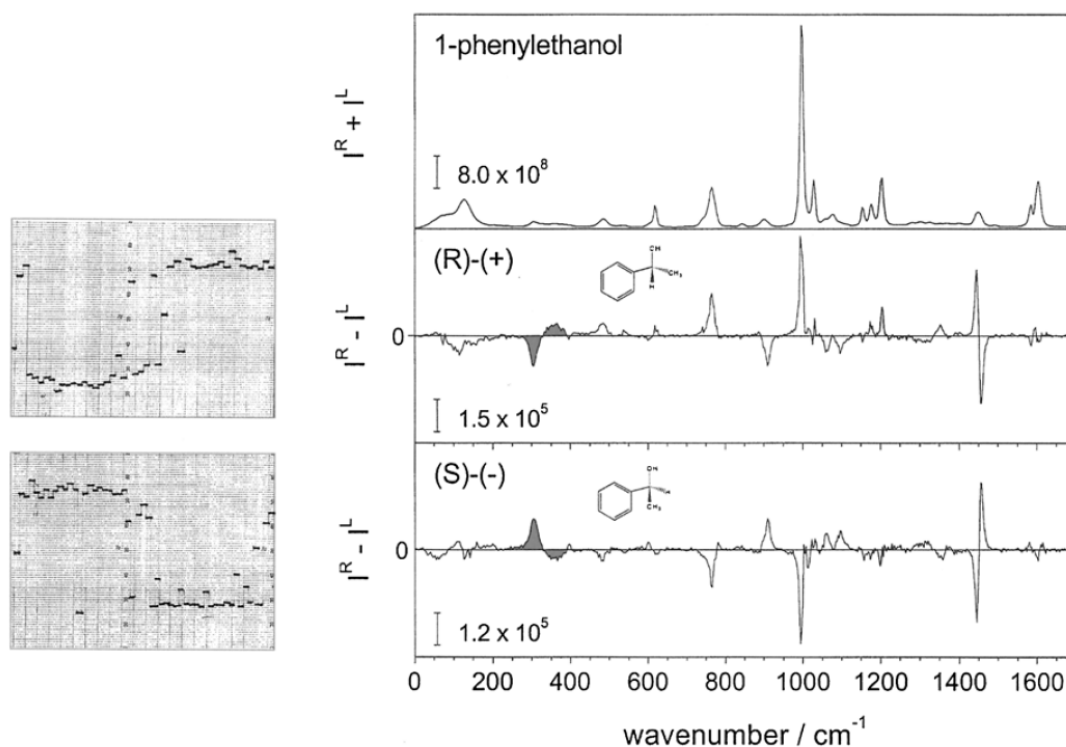
Figure 1.6: ROA spectra of two enantiomers of 1-phenylethanol. Left: the original 1972 observation in the range $\sim 290 - 400\,\mathrm{cm}^{-1}$. Right: Measurement from 2003, the reproduced couplets are shaded. From [Barron, 2015].

cell or a magnetic cell. On the other hand the software taking care of moving parts, camera readouts etc. is very convenient. To summarize, clear, isotropic, homogeneous liquid samples can be measured quite routinely, more complicated samples require special care.

Interpretaion of spectra. So far we have spoken about acquiring ROA spectra. But how can the lavish amount of information about molecular structure be obtained? If one is after absolute configuration or main structural motives (e.g. α-helix, β-sheet for proteins) consulting existing literature and comparing spectral shapes should suffice. But a much more systematic and universal approach is to resort to *ab initio* (from first principles) computational chemistry.

ROA spectral simulations from first principles. The first publication of an *ab initio*-calculated ROA spectrum appeared in 1989 [Bose et al., 1989]. The results presented therein were obtained within Hartree-Fock theory. A large improvement in accuracy came with the implementation of ROA calculations within density functional theory [Ruud et al., 2002] and further improvements are continuously being propelled by developments in quantum chemistry. When calculating spectra, many issues arise. Considerations need to be taken of solute-solvent interactions and effects of non-zero temperature, such as multiple conformer equilibria. Parallelization [Luber and Reiher, 2009], fragment-based *ab initio* [Jovan Jose and Raghavachari, 2016] or Cartesian tensor transfer [Yamamoto et al., 2012] techniques are contemporarily needed to make spectral simulations feasible for large molecules ($\sim 10^3$ –10^4 atoms).

Areas of ROA application. Today, measurement of **small chiral molecules** is quite straightforward, absolute configurations can often be assigned more easily than using "standard" methods (X-ray, NMR). In some cases, ROA is the only method available for absolute configuration determination [Haesler et al., 2007]. Perhaps surprisingly, interpretations of small molecule spectra by computations can be considerably complicated, because these molecules are often very flexible (not stabilized by intramolecular non-covalent bonding) and their interaction with the solvent has a profound effect on vibrational modes. Nevertheless, ROA studies of **peptides** and **proteins** are well established. Measurement is rather routine because they are soluble in water and stable in visible laser light. A study about conformational behaviour of a peptide appears in chapter 4. The Cartesian tensor transfer technique appears to be a promising approach to simulating spectra of proteins consisting of thousands of atoms, as was recently shown by Kessler et al. [2015]. **Saccharides** and **polysaccharides** do not possess chromophores absorbing in regions typical for electronic circular dichroism ($\sim 180 - 800 \, \text{nm}$) and thus vibrational optical activity is an appealing approach to study their chirality. Interpretation of polysaccharide spectra is extremely difficult due to flexibility of their structure and strong polar interactions with the solvent. Despite this, multiple successful interpretations have been made, e.g. by Kaminský et al. [2009] or Yaffe et al. [2010]. Less developed areas of ROA application are those of **nucleic acids** or **viruses**, though unique ROA fingerprints of several distinct structural motives have been reported [Hobro et al., 2008, Blanch et al., 2002].

Further ROA development. An intrinsic difficulty of ROA measurement is the weakness of the signals, typically only $\sim 10^{-4}$ of the Raman intensity, which is already small itself. The search for ways to improve instrumentation has definitely not ceased to an end. Also new mechanisms for signal enhancement are searched for. Some of these approaches try to take advantage of electronic resonance effects. This can be done by forming complexes of biomolecules with rare earth metals, such as europium, which provide low energy electronic states resulting in **induced-resonance ROA**. Another possibility is to move the exciting radiation to the UV region (**UV ROA**) or to attach molecules to metal surfaces (**surface-enhanced ROA**). For paramagnetic samples, and also diamagnetics with paramagnetic excited states, the chirality can be induced by a magnetic field (**magnetic ROA**) [Šebestík and Bouř, 2014].

Samples that are **inhomogeneous** on scales larger than the wavelength of light, such as powders, colloids or amyloid fibrils, are especially difficult to measure, because their inhomogeneity often results in irreproducible false signals. One of the goals of this thesis is to explore how these samples could be measured (chapter 5).

2. Experimental Aspects of ROA

The predominant difficulty in a Raman optical activity experiment is the weakness of the sought for signal. Spontaneous (non-resonant) Raman scattering itself is already an inefficient process. Even in condensed matter, passing light through a typical sample length of $\sim 1\,\mathrm{mm}$, only approximately 1 part in 10^7 will be scattered to a different (Stokes) frequency [Boyd, 2008]. An important experimental quantity for ROA, the circular intensity difference

$$\Delta = \frac{I_R - I_L}{I_R + I_L},\tag{2.1}$$

is typically of the order $10^{-5} - 10^{-3}$ [Li and Nafie, 2012], I_R and I_L are intensities of scattered right- and left-circularly polarized light. In total, if we think of the incident light intensity as a *haystack* of unit size, the size of the *needle* we are searching for is of the order $\sim 10^{-11}$.

Light Source and Detection. Not surprisingly then, ROA evaded observation until a powerful light source at a convenient wavelength and detector became available. Namely the argon ion laser operating at $488\,\mathrm{nm}$ and a Raman spectrometer equipped for photon counting was used for the original observation [Barron et al., 1973]. Today, the instruments of choice would be a frequency-doubled Nd^{3+}:YVO_4 (532 nm) laser and a back-thinned charge-coupled device (CCD) respectively.

Many factors are important when selecting an appropriate excitation wavelength. Firstly, the number of detectable photons in an ROA measurement N varies with wavelength λ as

$$N \propto \frac{1}{\lambda^4}\tag{2.2}$$

[Parchaňský et al., 2014], which dramatically favours short wavelengths, as in UV light.

A trouble with UV-ROA is that the Raman shift due to fundamental vibrations is only a few nanometers, while tens to hundreds are obtained for visible and infrared measurements, see figure 2.1 (page 14). This implies high demands on edge filters to block undesired Rayleigh scattering. Another issue is that resonance with electronic energy levels in measured samples becomes significant, which burdens interpretation. Also steady ultraviolet laser sources are not readily at one's disposal and samples may decompose under UV light.

A prevalent problem in the visible spectral range is fluorescence background from impurities in samples. The near infrared region would graciously circumvent the fluorescence problems. Raman fiber lasers are promising in this region and adequate detectors in the form of low-noise CMOS line scanners are expected in the near future [Hug, 2012]. A drawback for the long wavelengths is the dependence (2.2), which implies weak signals. High power irradiation is thus needed and consequently issues with sample overheating may arise.

To conclude, the excitation wavelength of 532 nm has established itself as a reasonable compromise between the points given above. Nonetheless, possibilities of other wavelengths in ROA measurement are also being explored (not within this thesis).
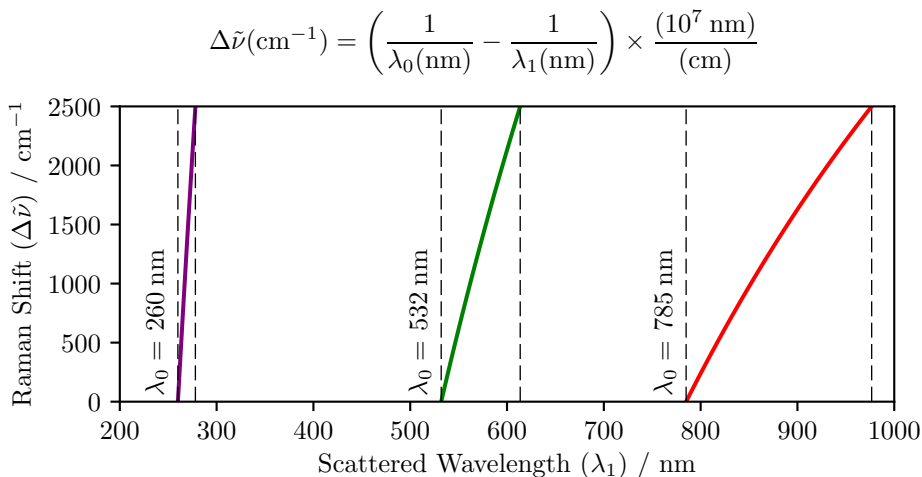
$$\Delta \tilde{\nu}(\text{cm}^{-1}) = \left(\frac{1}{\lambda_0(\text{nm})} - \frac{1}{\lambda_1(\text{nm})} \right) \times \frac{(10^7 \, \text{nm})}{(\text{cm})}$$

Figure 2.1: Dependence between scattered wavelength (λ_1) ranges for different excitation wavelengths (λ_0) and the Raman shift ($\Delta \tilde{\nu}$) range of $0 - 2500 \, \text{cm}^{-1}$.

In the remainder of this chapter, an account will be given for what happens between the source of light and the detector.

2.1 Overview of the Experimental Setup

In figure 2.2 (page 15) a scheme of a commonly used setup for ROA measurements can be found. ROA instruments have the same light sources, spectrographs and data acquisition systems as Raman instruments. Because ROA is a polarization spectroscopy, delicate care must be taken of all the elements affecting light polarization. Some details about possible scattering geometries, polarization modes, polarization conditioners and artefact suppression are given in the oncoming sections.

2.2 Scattering Geometry

The scattering geometry is defined by the angle θ between light incident on the sample and the direction in which scattered light is measured. Three basic scattering geometries are forward scattering ($\theta = 0$), right-angle scattering ($\theta = \pi/2$) and backward scattering ($\theta = \pi$). The first ROA instruments used the right-angle arrangement as this is the easiest to construct. However, the largest ROA/Raman ratio [eq. (2.1)] is obtained in backscattering and therefore this design is most frequent contemporarily [Nafie, 2011].

2.3 Polarization Modes

Independently of the scattering geometry, three distinct ways of handling polarized light within the apparatus exist. If the polarization of *incident* light is controlled and periodically switched between right- and left-circular, the polarization mode is termed ICP (incident circular polarization). Alternatively, if the incident
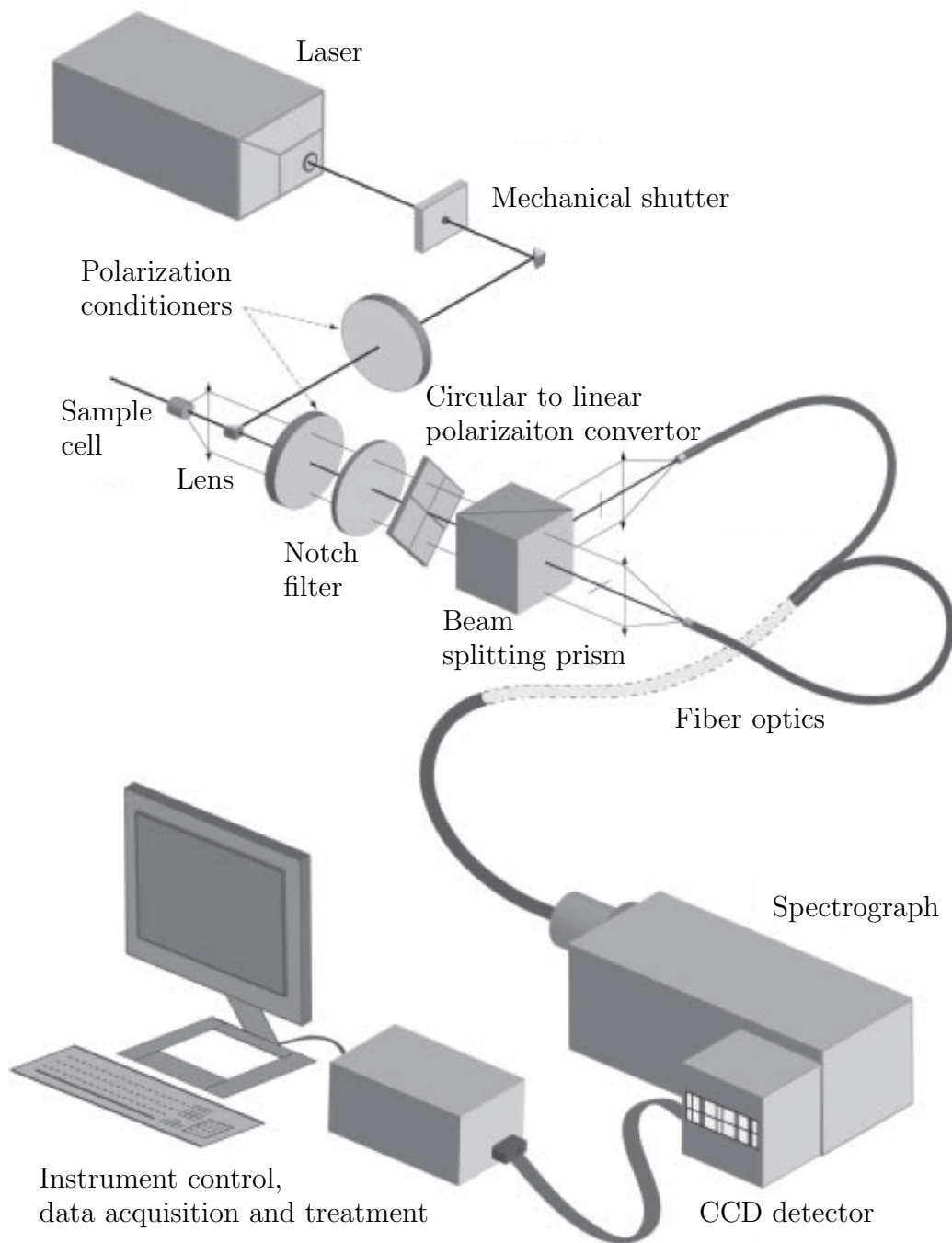
Figure 2.2: Building blocks of an SCP ROA spectrometer, adapted from [Hug, 2012].

light is unpolarized and the *scattered* light separated into its circular components, we refer to the setup as SCP. If *both* the incident and scattered polarization states are modulated and analyzed, the mode is termed DCP (dual circular polarization). The DCP mode can be further divided into *in phase* (DCP_I) and *out of phase* (DCP_II) depending on whether the incident component of circular polarization is the same or opposite to the detected component.

If the measured molecules satisfy the far-from-resonance limit and the back-scattering experiment is ideal, then

$$\text{ICP} = \text{SCP} = \text{DCP}_\text{I} \quad \text{and} \quad \text{DCP}_\text{II} = 0$$

[Li and Nafie, 2012]. However, deviation from the far-from-resonance approximation has been shown to increase with increasing electronic structure complexity and to be detectable already for α-pinene (figure 2.3).
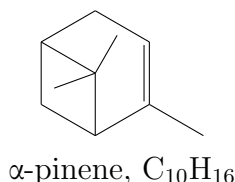

α-pinene, $C_{10}H_{16}$

Figure 2.3: A rather small molecule containing only one functional group absorbing near the excitation wavelength; the double bond. Yet it already gives different ROA signals in ICP, SCP and DCP_I, and non-zero DCP_II. Reported by Yu and Nafie [1994].

This leads to non-zero DCP_II and non-equivalence of the other polarization modes already on a theoretical basis [Nafie, 2008].

Further differences arise from specific construction details. An advantage of the ICP setup is that handling of the polarization takes place before the scattering event when the light is still monochromatic, making the polarization conditioners more effective. On the other hand, SCP gains significantly from the fact that both states of circular polarization are measured simultaneously, from the same focal volume at the same instant of time. All fluctuations in laser power, sample density, in the optical path (e.g. dust particles) or heat fluctuations of the detector cancel out.

2.4 Eliminating Deterministic Offsets

Apart from experimental noise, an important source of offset in an optical activity measurement is *deterministic offset*. By this we mean unfluctuating imperfections of the apparatus, such as undesired birefringence of mirrors, lenses, sample cells etc.

Linear Polarization Scrambling

To produce unpolarized incident light in the SCP setup, typically a linearly polarized light is rotated. This is achieved by two counter-rotating half-wave plates.

This not only doubles the polarization plane rotation speed (typically reaching ~ 50 kHz), but also eliminates offsets caused by the differences in wave plate transmission with respect to their orientation to the plane of polarization. Ideally, the linear polarization scrambling is synchronized with the data acquisition cycle [Hug, 2012].

Mirror Couplets

When the state of light polarization upon a right-angle reflection is to be preserved, it is advantageous to use a pair of mirrors instead of one, as illustrated in figure 2.4. The arrangement is such that the p-polarization component (*in* the plane of reflection) in the first reflection becomes the s-polarization component (*perpendicular* to the plane of reflection) the second time, and vice versa.
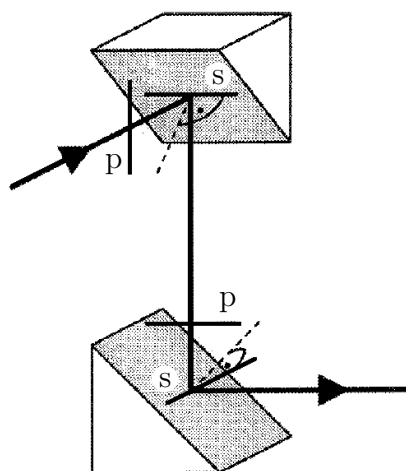

Figure 2.4: Reflection from a pair of mirrors. The p- and s-polarization states are switched to compensate for depolarization. From [Hug and Hangartner, 1999].

The Virtual Enantiomer

A possibility to almost entirely eliminate deterministic offset in an optical activity measurement is to measure both enantiomers of the sample. By subtracting their signals one obtains the offset. However, this is not an option for the vast majority of biomolecules, because both enantiomers are not reasonably obtainable. A rather simple, yet remarkably powerful solution came from Hug [2003]. A half-wave plate acts as a circularity convertor for circularly polarized light and rotates linearly polarized light by twice the angle between the half-wave fast axis and the direction of polarization. A sample placed between two half-wave plates viewed from the outside thus appears as its enantiomer.

A typical optical setup for creating the so called *virtual enantiomer* is schematically depicted in figure 2.5 (page 18).
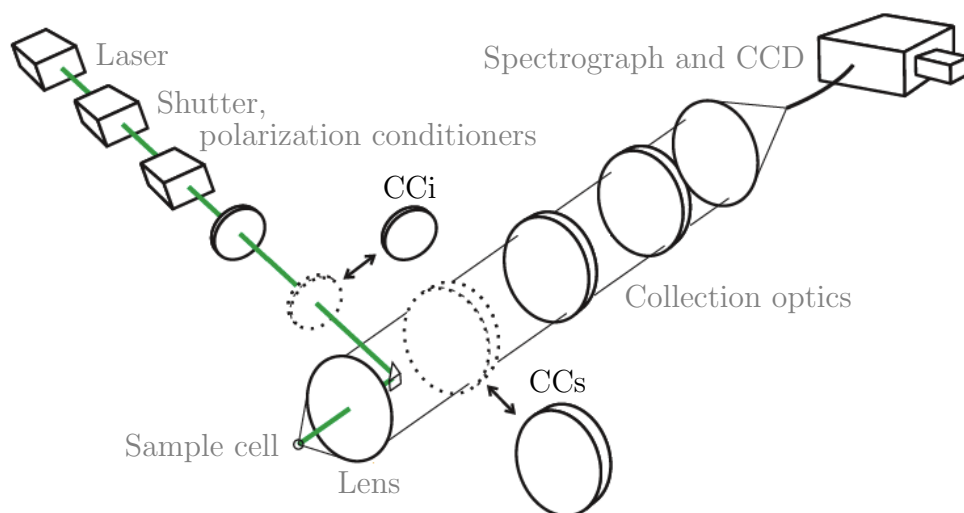
Figure 2.5: The virtual enantiomer setup. Incident (CCi) and scattered (CCs) circularity converters / half-wave plates are positioned in or out of the optical path. If in, this practically makes the sample appear as its mirror image. Adapted from [Yamamoto and Watarai, 2010].

3. Theoretical Aspects of ROA

Exploitation of the complex information obtained from vibrational spectroscopy requires elaborate spectral interpretation. Simple rules-of-thumb, e.g. the octant rule for analyzing rotary strengths of circular dichroism [Eliel and Wilen, 2008], or parametrization methods have proven not to be viable. One thus resorts to interpreting spectra from first principles. A brief overview and some practical issues are discussed in this chapter.

3.1 ROA Circular Intensity Difference and Related Variables

Before we begin, please note that throughout this chapter Latin indices are used to number particles (nuclei, electrons), Greek indices label Cartesian coordinates (x, y and z) and the Einstein summation convention (using only subscripts) is assumed for the Greek indices, $\delta_{\alpha\beta}$ and $\varepsilon_{\alpha\beta\gamma}$ are the Kronecker delta and Levi-Civita symbol. The treatment and notation conventions presented in this section closely follow those of Barron and Buckingham [2010] and Barron [2004].

To give an account for the molecular origin of optical activity phenomena, it is necessary to include higher multipole moments of molecules than just the electric dipole $\boldsymbol{\mu}$. Specifically, couplings of the electric dipole with the magnetic dipole $\boldsymbol{m}$ and (traceless) electric quadrupole $\boldsymbol{\Theta}$ are the key contributions. In SI units, these multipole moments are defined as

$$\mu_\alpha = \sum_i e_i r_{i\alpha},$$

$$m_\alpha = \sum_i \frac{e_i}{2m_i}\varepsilon_{\alpha\beta\gamma}r_{i\beta}p_{i\gamma},$$

$$\Theta_{\alpha\beta} = \frac{1}{2}\sum_i e_i\left(3r_{i\alpha}r_{i\beta} - \boldsymbol{r}_i^2\delta_{\alpha\beta}\right),$$

where e_i, m_i, $\boldsymbol{r}_i$ and $\boldsymbol{p}_i$ are charge, mass, position and momentum of particle i. The electric and associated magnetic field of a plane-wave light beam of frequency $\omega = 2\pi c/\lambda$ and wavevector $\boldsymbol{k} = 2\pi\boldsymbol{n}/\lambda$ are

$$\boldsymbol{E} = \boldsymbol{E}^0\cos(\boldsymbol{k}\cdot\boldsymbol{r} - \omega t),$$

$$\boldsymbol{B} = \frac{1}{c}\boldsymbol{n}\times\boldsymbol{E}.$$

These fields induce changes of the molecular charge distribution. In the far-from-resonance approximation these can be quantified as

$$\langle\mu_\alpha\rangle = \alpha_{\alpha\beta}E_\beta + \frac{1}{\omega}G'_{\alpha\beta}\dot{B}_\beta + \frac{1}{3}A_{\alpha,\beta\gamma}\partial_\beta E_\gamma + \cdots,$$

$$\langle m_\alpha\rangle = -\frac{1}{\omega}G'_{\beta\alpha}\dot{E}_\beta + \cdots,$$

$$\langle\Theta_{\alpha\beta}\rangle = A_{\alpha,\beta\gamma}E_\gamma + \cdots,$$

where the angle brackets denote quantum-mechanical expectation values ($\langle\mu_\alpha\rangle \equiv \langle\psi|\mu_\alpha|\psi\rangle$, $|\psi\rangle$ is the molecular wavefunction), $\boldsymbol{\alpha}$, $\boldsymbol{G'}$ and $\boldsymbol{A}$ are refered to as molecular property tensors. For Raman scattering we need to consider the following expressions obtained from time-dependent perturbation theory.

$$\alpha_{\alpha\beta} = \frac{2}{\hbar}\sum_{j\neq n}\frac{\omega_{jn}}{\omega_{jn}^2 - \omega^2}\mathrm{Re}\left(\langle n|\mu_\alpha|j\rangle\,\langle j|\mu_\beta|f\rangle\right) \tag{3.1a}$$

"el. dipole – el. dipole polarizability tensor"

$$G'_{\alpha\beta} = -\frac{2}{\hbar}\sum_{j\neq n}\frac{\omega}{\omega_{jn}^2 - \omega^2}\mathrm{Im}\left(\langle n|\mu_\alpha|j\rangle\,\langle j|m_\beta|f\rangle\right) \tag{3.1b}$$

"el. dipole – mag. dipole polarizability tensor"

$$A_{\alpha,\beta\gamma} = \frac{2}{\hbar}\sum_{j\neq n}\frac{\omega_{jn}}{\omega_{jn}^2 - \omega^2}\mathrm{Re}\left(\langle n|\mu_\alpha|j\rangle\,\langle j|\Theta_{\beta\gamma}|f\rangle\right) \tag{3.1c}$$

"el. dipole – el. quadrupole polarizability tensor"

Here n, j and f label the initial, excited and final states of the molecule respectively, and $\omega_{jn} = \omega_j - \omega_n$.

As was mentioned in the beginning of chapter 2, an important experimental quantity for ROA is the circular intensity difference (CID)

$$\Delta = \frac{I_R - I_L}{I_R + I_L}.$$

Molecular expressions for CIDs may be developed semiclassically by writing down the electric field vector radiated by the oscillating electric dipole, magnetic dipole and electric quadrupole moments induced by right- and left-circularly polarized light. For the example of the most commonly used experimental setup, backscattering ($\theta = \pi$) SCP (see page 14), the expression for the CID is

$$\Delta^{SCP}(\pi) = \frac{8\left(3\alpha_{\alpha\beta}G'^*_{\alpha\beta} - \alpha_{\alpha\alpha}G'^*_{\beta\beta} + \frac{1}{3}\omega\alpha_{\alpha\beta}\varepsilon_{\alpha\gamma\delta}A^*_{\gamma,\delta\beta}\right)}{c\left(7\alpha_{\lambda\mu}\alpha^*_{\lambda\mu} + \alpha_{\lambda\lambda}\alpha^*_{\mu\mu}\right)}.$$

The only task that remains is to calculate the molecular property tensors. Their sum-over-states definition given in equations (3.1) is not commonly used for calculations, since it would require knowledge of all excited molecular states $|j\rangle$. Instead, an energy differentiation approach is typically used.

For electrically neutral molecules in uniform static fields, by Taylor expanding the energy in terms of field components one can arrive at equations for the molecular property tensors involving energy derivatives, e.g.

$$\alpha_{\alpha\beta} = -\frac{\partial^2}{\partial E_\alpha \partial E_\beta}\langle\psi|H_{\mathrm{mol}} + H_{\mathrm{EM}}^{\mathrm{classical}}|\psi\rangle\,, \tag{3.2}$$

where H_{mol} is the molecular Hamiltonian and $H_{\mathrm{EM}}^{\mathrm{classical}}$ the electromagnetic field contribution treated classically. In the case of dynamic fields we are interested in, the situation becomes more involved, although in the end it comes down to evaluating energy derivatives as in (3.2). The techniques are reviewed in [Ruud, 2012] or [Ruud and Thorvaldsen, 2009].

3.2 *Ab Initio* Computational Chemistry

To calculate the molecular property tensors from energy derivatives [such as (3.2)], the wavefunction $|\psi\rangle$ of the studied system must be known. Solving the time-independent Schrödinger equation for molecules is the task of *ab initio* (from first principles) computational chemistry. As this field of study is vast and fairly complex, a review is not attempted here. Only concepts relevant to vibrational analysis will be introduced in the remainder of this chapter. A broader introduction to *ab initio* computational chemistry can be found in a bachelor's thesis by Jungwirth [2014], standard reference texts are Szabo and Ostlund [1996] for Hartree-Fock, Koch and Holthausen [2015] for density functional theory (DFT).

The Born-Oppenheimer Approximation. Central to most of contemporary quantum chemistry, and important to vibrational analysis, is the Born-Oppenheimer approximation (BOA), which decouples nuclear and electronic motion on the basis of the large disproportionality between their masses. The idea is that the "heavy" nuclei move "slowly", so they appear to be static to the "light", "fast moving" electrons. The electrons therefore "instantaneously" adapt to any change in nuclei positions.

To restate that in the language of equations, we begin with the time-independent Schrödinger equation

$$H \left|\psi\right\rangle = E \left|\psi\right\rangle, \tag{3.3}$$

$$H = T_\mathrm{n} + \underbrace{T_\mathrm{e} + V}_{H_\mathrm{e}},$$

where H is the total molecular Hamiltonian consisting of nuclear and electronic kinetic energy terms (T_n, T_e), and the electrostatic energy contributions V. The last two Hamiltonian terms have been grouped together into an "electronic" part H_e. E is an energy eigenvalue and $|\psi\rangle$ is the total molecular wavefunction. Next we introduce an ansatz of BOA, that $|\psi\rangle$ may be factored into nuclear and electronic components

$$\left|\psi\right\rangle = \left|\psi_\mathrm{n}(\boldsymbol{R})\right\rangle \left|\psi_\mathrm{e}(\boldsymbol{r}, \boldsymbol{R})\right\rangle. \tag{3.4}$$

Part of this ansatz is that the nuclear part depends only on the set of nuclear positions $\boldsymbol{R}$, not on the set of electronic positions $\boldsymbol{r}$. The electronic part naturally depends on both. Now, for *fixed* nuclei positions, acting with H_e on the electronic wavefunction we get

$$H_\mathrm{e} \left|\psi_\mathrm{e}\right\rangle = E_\mathrm{e}(\boldsymbol{R}) \left|\psi_\mathrm{e}\right\rangle, \tag{3.5}$$

where the electronic energy eigenvalues E_e parametrically depend on the given nuclei positions $\boldsymbol{R}$. Equation (3.5) is often referred to as the *electronic structure problem*. BOA continues with the assumption that operation of the nuclear kinetic energy operator on the electronic wavefunction may be neglected

$$T_\mathrm{n} \left|\psi_\mathrm{e}\right\rangle = 0. \tag{3.6}$$

Now putting together what we got in equations (3.4), (3.5) and (3.6) into the

Schrödinger equation (3.3) we obtain

$$H \left| \psi \right\rangle = E \left| \psi \right\rangle$$

$$(T_{\mathrm{n}} + H_{\mathrm{e}}) \left| \psi_{\mathrm{n}}(\boldsymbol{R}) \right\rangle \left| \psi_{\mathrm{e}}(\boldsymbol{r}, \boldsymbol{R}) \right\rangle = E \left| \psi_{\mathrm{n}}(\boldsymbol{R}) \right\rangle \left| \psi_{\mathrm{e}}(\boldsymbol{r}, \boldsymbol{R}) \right\rangle$$

$$[T_{\mathrm{n}} + E_{\mathrm{e}}(\boldsymbol{R})] \left| \psi_{\mathrm{n}}(\boldsymbol{R}) \right\rangle \left| \psi_{\mathrm{e}}(\boldsymbol{r}, \boldsymbol{R}) \right\rangle = E \left| \psi_{\mathrm{n}}(\boldsymbol{R}) \right\rangle \left| \psi_{\mathrm{e}}(\boldsymbol{r}, \boldsymbol{R}) \right\rangle. \qquad (3.7)$$

On the last line [equation (3.7)], no operator acts on the electronic wavefunction, so it may be dropped. The final form is referred to as the *nuclear structure problem*.

$$\underbrace{[T_{\mathrm{n}} + E_{\mathrm{e}}(\boldsymbol{R})]}_{H_{\mathrm{n}}} \left| \psi_{\mathrm{n}}(\boldsymbol{R}) \right\rangle = E \left| \psi_{\mathrm{n}}(\boldsymbol{R}) \right\rangle, \qquad (3.8)$$

H_{n} being the nuclear Hamiltonian. From this we see that the electronic energy obtained from solving the electronic structure problem [E_{e} from (3.5)] takes the role of a *potential* in the nuclear structure equation (3.8).

Potential energy surface, harmonic approximation. Having separated the nuclear and electronic motions, we may think of the nuclei as objects moving on a "potential energy surface" (PES) $E_{\mathrm{e}}(\boldsymbol{R})$, where $\boldsymbol{R} \equiv \{R_i\}$ is the set of nuclear coordinates. Finding local minima $E_{\mathrm{e}}(\{R_i^0\})$ on this surface is a task for quantum chemistry, vibrational motion is then governed by the PES shape in the vicinity of minima. As the dimensionality of this surface (three times the number of nuclei) can be relatively large, it is most often somewhat approximated. The harmonic approximation (3.9) takes only terms up to second order.

$$E_{\mathrm{e}}(\{R_i\}) = E_{\mathrm{e}}(\{R_i^0\}) \qquad \ldots \text{a constant} \qquad (3.9\mathrm{a})$$

$$+ \sum_j \left[\frac{\partial E_{\mathrm{e}}(\{R_i\})}{\partial R_j} \Big|_{R_j = R_j^0} \right] \left(R_j - R_j^0 \right) \quad \ldots = 0 \text{ at minimum} \quad (3.9\mathrm{b})$$

$$+ \frac{1}{2} \sum_{j,k} \left[\frac{\partial^2 E_{\mathrm{e}}(\{R_i\})}{\partial R_j \partial R_k} \Big|_{\substack{R_j = R_j^0 \\ R_k = R_k^0}} \right] \left(R_j - R_j^0 \right) \left(R_k - R_k^0 \right) \qquad (3.9\mathrm{c})$$

$$+ O(R_i R_j R_k) \qquad \ldots \text{ommited.} \qquad (3.9\mathrm{d})$$

The harmonic approach is known to give satisfactory results for most of the lower frequency vibrations ($200 - 1800 \, \mathrm{cm}^{-1}$) [Daněček et al., 2007].

To obtain vibrational frequencies and to visualize vibrational modes, diagonalization of the hessian [energy second derivatives as in (3.9c)] is performed.

$$\begin{pmatrix} \ddots & & \iddots \\ & \frac{\partial^2 E_{\mathrm{e}}(\{R_i\})}{\partial R_j \partial R_k} \Big|_{\substack{R_j = R_j^0 \\ R_k = R_k^0}} & \\ \iddots & & \ddots \end{pmatrix} = \boldsymbol{S} \begin{pmatrix} \omega_1^2 & & 0 \\ & \ddots & \\ 0 & & \omega_n^2 \end{pmatrix} \boldsymbol{S}^{-1}.$$

$\boldsymbol{S}$ is the transformation matrix between Cartesian and normal mode coordinates, each normal mode is characterized by its frequency ω (or wavenumber $\tilde{\nu} = \omega/2\pi c$).

Methods, basis sets, software. As far as the electronic problem (3.5) is concerned, all simulations were performed using hybrid functionals (DFT). The systems studied were too large to employ more accurate wavefunction methods, e.g. coupled clusters. It has been observed, that diffuse basis functions both for hydrogen and the "heavy" atoms (C, N, O, S, . . .) in calculations significantly improve predicted spectra [Pecul and Rizzo, 2003, Hug, 2001]. The reason for this is believed to be that electrons far from nuclei considerably affect molecular vibrations. Polarization functions (e.g. p-orbitals for hydrogen) are standardly included to increase basis set flexibility.

For all practical purposes, calculation of ROA intensities has been implemented in a number of *ab initio* programs, notably Gaussian [Frisch et al., 2013], Dalton [Aidas et al., 2014] or Turbomole [Ahlrichs et al., 1989].

3.3 Modelling Solvent and Temperature Effects

What was advocated in chapter 1 as an asset, that ROA can be measured in aqueous solvent, becomes a strain for spectra simulations. The polar water molecules often interact significantly with investigated biomolecules affecting their conformation, charge distribution and vibrational modes. Therefore, including solvent effects in the theoretical model is needed, especially for polar molecules.

Another shortcoming of quantum chemical calculations is that they take place at $0\,\mathrm{K}$. Temperature brings with it conformational dynamics of the entire system. Multiple conformations of the solute may be present in accord with the Boltzmann distribution[1] and each conformation may contribute differently to the spectrum. Also solvent molecules are in ceaseless thermal motion and, again, each layout of these molecules around the sample results in a different contribution to the spectrum.

There are two main approaches to solvent modelling, often termed *implicit* and *explicit*, see figure 3.1 (page 24). So called implicit models place the studied molecule in a cavity surrounded by a polarizable continuum. In explicit models, a limited number of solvent molecules are also treated quantum mechanically. Most commonly, the combined system in explicit models (often termed a cluster) is also embedded in a polarizable continuum as this does not add significantly to the computational demands. It has been shown before that implicit models may suffice for obtaining reasonable energies and structures [Cossi et al., 2003], but explicit models appear indispensable for an adequate description of vibrational frequencies of polar groups, and thus they often significantly improve spectra predictions for vibrational Raman and ROA [Hopmann et al., 2011].

To obtain such "solvated clusters" (as in figure 3.1b), one often resorts to molecular dynamics (MD)[2] by which a solvent bath of substantial size may be modelled. By taking many snapshots from MD simulations, an ensemble of possible solvent positions and solute conformations is obtained.

---

[1]The probability of a conformer specified by the set of nuclear coordinates $\boldsymbol{R}$ is $p(\boldsymbol{R}) \propto \exp(-E(\boldsymbol{R})/k_B T)$, where $E(\boldsymbol{R})$ is its energy [approximated as $E_\mathrm{e}(\boldsymbol{R})$ from (3.5)], k_B the Boltzmann constant and T the temperature.

[2]Molecular dynamics is a method for studying motion of atoms and molecules by numerically solving Newton's equations of motion.

(a) $|\psi\rangle$ in an implicit solvent model

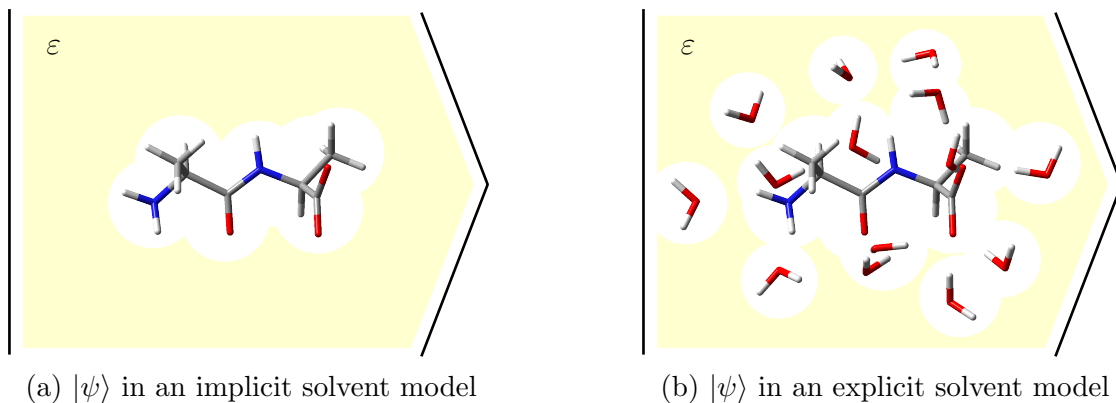(b) $|\psi\rangle$ in an explicit solvent model

Figure 3.1: Systems in implicit (a) and explicit (b) solvent models. In both cases, the molecules are embedded in a polarizable continuum model (▢) with permitivity ε.
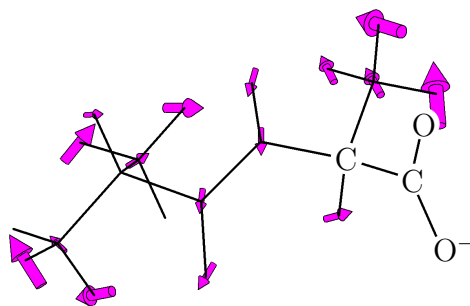
3.3.1 Normal Mode Optimization

With the solvated clusters, solvent and temperature effects have been included in the model to some extent. However, these clusters may be far from energy minima on the (quantum mechanical) potential energy surface (3.9), and spectra predicted directly from these may be unreliable [Hopmann et al., 2011]. Further optimization is needed, but by resorting to a full *ab initio* optimization (at 0 K), one would lose most of the dynamical information brought in by MD.

A viable approach to constrained optimization is the *normal mode* technique introduced to vibrational spectroscopy by Bouř and Keiderling [2002]. In normal modes, there is an elegant separation between the low frequency modes containing the majority of torsional and solvent molecule movement, and the high frequency modes which are mainly measured by vibrational spectroscopy and need to be optimized, see figure 3.2. There is some ambiguity in where exactly is the boundary between constrained and relaxed modes, and it depends on the system studied. The typical value is between $100 - 300 \, \mathrm{cm}^{-1}$.
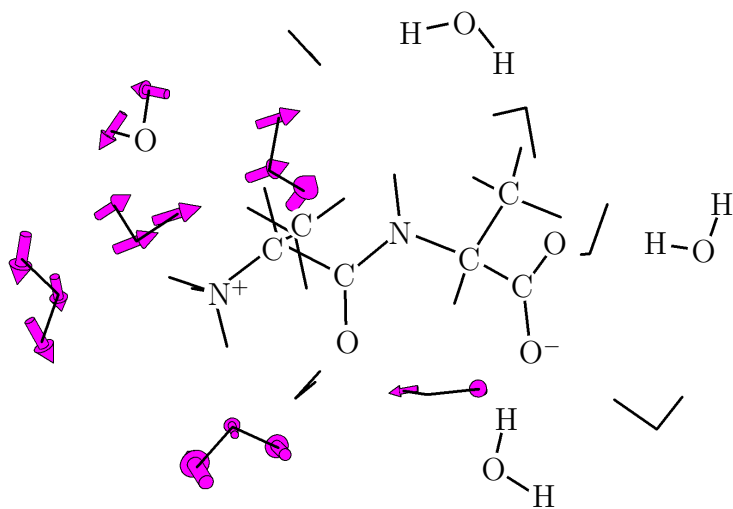
(a) $\omega \propto 40\,\mathrm{cm}^{-1}$, mainly water (solvent) translation and rotation, typically *fixed* in a normal mode optimization.

(b) $\omega \propto 135\,\mathrm{cm}^{-1}$, mainly skeletal deformation, typically *fixed* in a normal mode optimization.
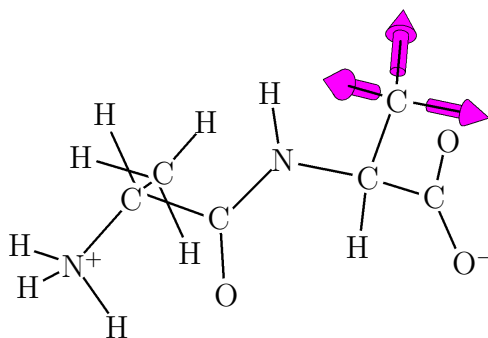
(c) $\omega \propto 3037\,\mathrm{cm}^{-1}$, –CH$_3$ stretching, typically *relaxed* in a normal mode optimization.

Figure 3.2: Vibrational modes of a dialanine-water cluster (a) and dialanine (b, c). Illustrates the character of various low (a, b) and high (c) frequency modes and how they are treated in the normal mode optimization procedure.

4. Conformational Behaviour of L-Alanyl-L-Alanine Investigated by ROA

L-alanyl-L-alanine is a molecule consisting of two chiral amino acid monomers bound together by the amide bond (figure 4.1). Since we will only be dealing with the L- enantiomer, we shall mostly refer to the molecule just as dialanine or Ala-Ala. The molecule is well suited as a "minimal" peptide model, and has been studied before to unravel basic properties of the amide group in larger peptides [Oboodi et al., 1984, Šebek et al., 2007, Yu et al., 1995]. Vibrational coupling of the two alanine side chains results in a strong ROA signal providing valuable information about secondary structure of the main peptide chain [Barron and Buckingham, 1974, Herrmann et al., 2006, Yamamoto et al., 2014].

In some sense, spectroscopic studies of such short peptides are more complicated than of longer peptide chains. The longer chain structures usually stabilize by intermolecular non-covalent bonding resulting in an unchanging backbone conformation (secondary structure) [Sreerama and Woody, 2000]. Such stabilization is limited in short peptides, therefore segments of the molecule can rotate with relative ease around backbone single bonds. As a result multiple conformers are present at room temperature. Also, solute-solvent interactions, such as hydrogen bonding, are more pronounced for smaller polar molecules. Accounting for the conformational dynamics and solvent effects in theoretical modelling can be significantly improved by employing combined quantum mechanics / molecular dynamics (QM/MM) procedures [Choi and Cho, 2009, Hopmann et al., 2011].

Changes of pH, which result in protonation of the peptide C-terminus in acidic environment (figure 4.1a) or deprotonation at the N-terminus in basic solution (figure 4.1c), are known to have an effect on the conformer equilibria [Jalkanen et al., 2003]. The small size of dialanine along with its conformational flexibility,
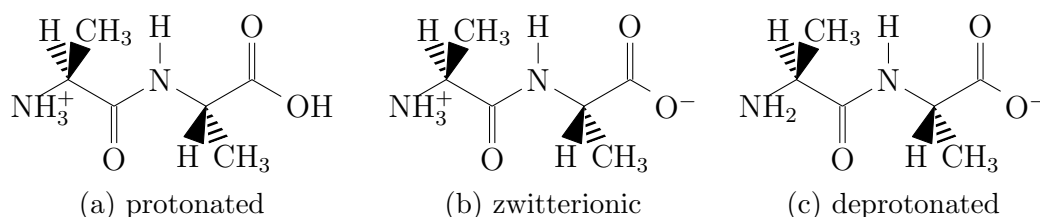
(a) protonated   (b) zwitterionic   (c) deprotonated

Figure 4.1: L-alanyl-L-alanine (dialanine, Ala-Ala) in aqueous solution. (a): acidic solution, pH $\approx$ 1. (b): neutral solution, pH $\approx$ 7. (c): basic solution, pH $\approx$ 13.

strong ROA signal and chemical similarity to larger peptides make it a useful model for testing methods of spectra interpretation. Multiple spectroscopic studies of dialanine have been done before [Weir et al., 2001, Jalkanen et al., 2003, Šebek et al., 2009] and have revealed interesting stuctural information. Visual comparison of simulated and experimental spectra, or a mathematical decomposition of experimental spectra into simulated spectra of individual conformers can provide information about conformer equilibria [Parchaňský et al., 2013].

However, as far as we know, practical accuracy and numerical stability of such procedure have not yet been extensively addressed.

4.1 Objectives

In comparison to previous Raman and ROA studies of the dialanine molecule we use a combined QM/MM theoretical approach. By this we attempt to improve experiment interpretation in order to be able to assign a higher number of spectral features. We further test if our results have reached such quality that a decomposition of the experimental spectrum into calculated spectra could provide reliable information about conformational equilibria.

To verify our (model dependent) results, we look into how accurately we can follow spectral changes upon changes in pH. Also, we prepared and measured spectra of two deuterated species of dialanine (figures 4.2b and 4.2c). Deuterium

(a) natural (d0-) Ala-Ala   (b) d2-Ala-Ala   (c) d8-Ala-Ala
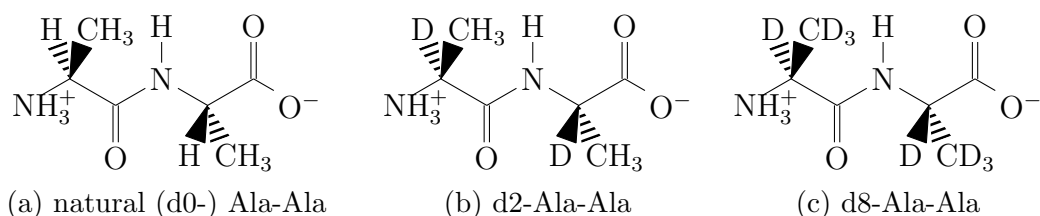
Figure 4.2: Zwitterionic L-alanyl-L-alanine at various levels of deuteration, i.e. exchange of hydrogen for deuterium (^{1}H $\equiv$ H $\leftrightarrow$ ^{2}H $\equiv$ D).

atoms have an identical electronic structure to hydrogen, so their presence does not affect conformation significantly. Their nearly double mass, however, has a profound effect on vibrational motion and thus different spectra result, as illustrated in figure 4.3.
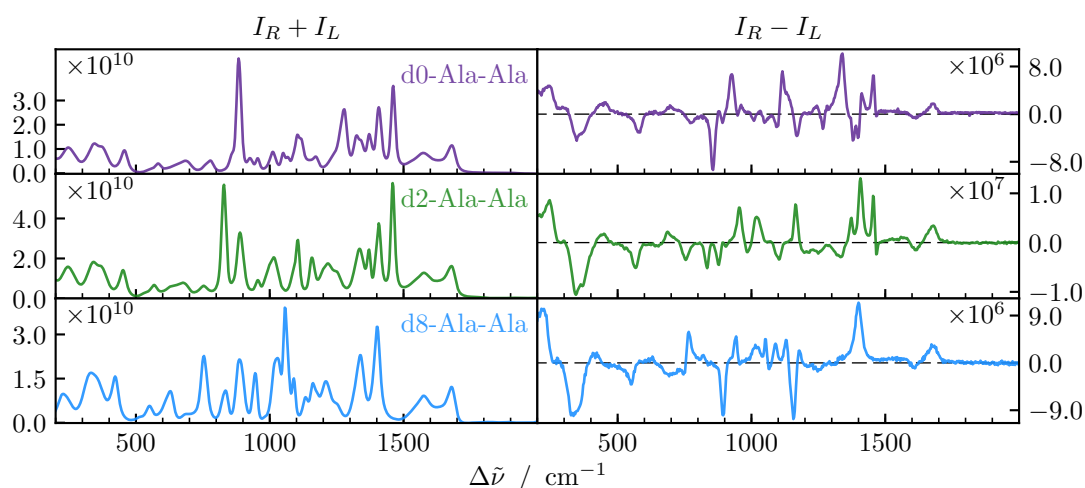

Figure 4.3: Spectral changes upon deuteration of zwitterionic dialanine, Raman (left) and ROA (right). Intensities are given in instrumental units.

4.2 Methods

Experimental spectra. L-alanyl-L-alanine was obtained commercially from Sigma-Aldrich, d2- and d8- molecules (figure 4.2) were synthesized from isotopically labeled alanine (Sigma-Aldrich) using a procedure found in [Bouř et al., 2005a]. Raman and ROA spectra were collected using a backscattering BioTools μ-ChiralRAMAN-2X [Hug and Hangartner, 1999, Hug, 2003] instrument in the scattered circular polarization (SCP) arrangement equipped with a 532 nm laser (Laser Quantum Opus 2 W). The peptides were dissolved at concentrations of $100\,\mathrm{mg\,ml^{-1}}$ in water, pH adjustments were done with HCl to pH 1.3 or NaOH to pH 12. Laser power at the sample was $330-560\,\mathrm{mW}$ and acquisition times were $12-33$ hours. All samples were measured in a 4×3 mm fused silica rectangular cell at room temperature (298 K). A spectrum of the solvent was subtracted from all Raman spectra. Baseline in some Raman and ROA spectra was also corrected by a polynomial fit. The frequency was calibrated using a neon lamp, the intensity was calibrated using a standard fluorescence reference material[1].

Molecular dynamics. Protonated, zwitterionic and deprotonated dipeptide were each put in a 30 Å cubic box filled with water molecules. After 1 ns equilibration, production MD was run for 1 ns using the Amber10 [Case et al., 2005] software package, Amber03 force field [Best and Hummer, 2009], NTV thermodynamic ensemble, temperature of 300K, 1fs integration step and periodic boundary conditions. In addition to restraint-free dynamics, the weighted histogram analysis method (WHAM) [Kumar et al., 1992] was used to investigate the free energy within the full space of the two most important torsional angles. During the free dynamics, snapshots of the geometry were saved every 1 ps, divided according to conformation and used for spectra generation.

Computation of Raman and ROA Spectra. For 100 snapshots of each conformer, level of protonation and isotopically labeled form, spectra were generated within the harmonic approximation. Firstly, water molecules further than 3.6 Å from the peptide were deleted. Then the geometries of remaining clusters containing the peptide and $11-17$ water molecules were partially optimized in vibrational normal mode coordinates [Sellers et al., 1978, Bouř and Keiderling, 2002]. Modes with frequencies under $250\,\mathrm{cm^{-1}}$ were fixed. This procedure ensures that the MD geometry is approximately conserved, while the vibrational modes important for the spectra are relaxed [Hudecová et al., 2011]. The Qgrad program [Bouř and Keiderling, 2002] interfaced to the Gaussian software package [Frisch et al., 2013] was used for the partial optimization performed at the B3PW91/6-311++G** level of theory and with the conductor-like polarizable continuum solvent model (COSMO) [Klamt, 1998, Cances et al., 1997] accounting for not explicitly included water. After the optimization, harmonic frequencies and Raman and ROA intensities were calculated by Gaussian at the same level. Theoretical spectra were obtained by convolution with Lorentzian bands of $10\,\mathrm{cm^{-1}}$ full-width at half-maximum.

---

[1]Standard Reference Material 2242 (https://www-s.nist.gov/srmors/certificates/2242.pdf)

4.2.1 Spectral Decomposition

Experimental Raman and ROA spectra (S_{exp}) are presumed to be linear combinations of calculated conformer spectra (S_i)

$$S_{\mathrm{exp}}(\omega) = \sum_i c_i S_i(\omega'), \tag{4.1a}$$

$$\text{with} \quad c_i \geq 0 \quad \text{and} \quad \sum_i c_i = 1. \tag{4.1b}$$

The frequencies of calculated spectra were linearly transformed ("scaled") to maximize the overlap between calculated and experimental spectra and thus correct the systematic computational error [Polavarapu and Covington, 2014]. Coefficients of the transformation are given in equation 4.2 and the effect is illustrated in figure 4.4.

$$\omega' = a\omega + b, \quad \text{with} \quad a = 0.969 \quad \text{and} \quad b = 19.0\,\mathrm{cm}^{-1} \tag{4.2}$$
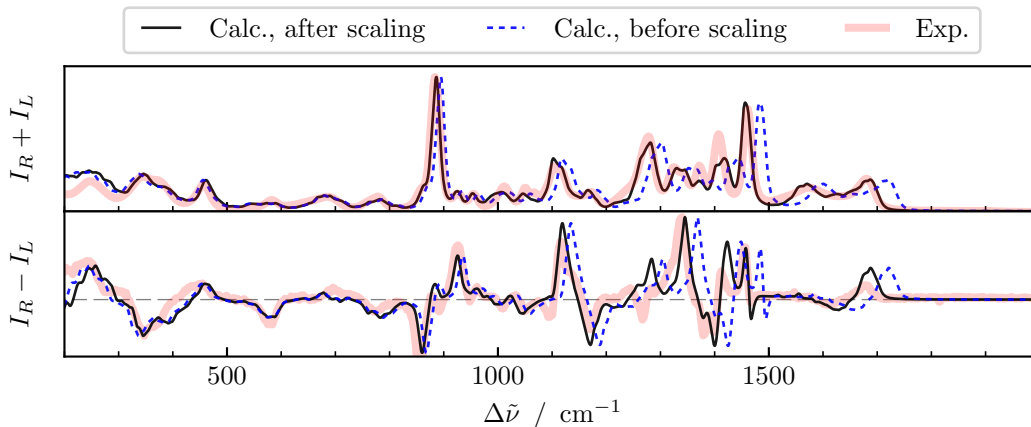
Figure 4.4: The effect of a frequency linear transformation in calculated spectra, experimental spectrum illustrated in the background. $\omega \propto \Delta\tilde{\nu}$ (Raman shift).

The conformer coefficients were obtained by minimizing the difference function δ,

$$\delta = \int_{\omega_{\mathrm{min}}}^{\omega_{\mathrm{max}}} d\omega \left[S_{\mathrm{exp}}(\omega) - \sum_i c_i S_i(\omega') \right]^2, \tag{4.3}$$

by scanning the $(c_1, c_2, \ldots, c_n)$ coefficient space, $(\omega_{\mathrm{min}}, \omega_{\mathrm{max}})$ is the relevant spectral range, we used $(300, 1900)\,\mathrm{cm}^{-1}$. Unlike usual minimization methods (Lagrange multipliers, singular value decomposition), the direct scanning allows to satisfy the conditions imposed on c_i in equation (4.1b) without any additional penalty functions. Also, this approach allows to easily look into smoothness of the coefficient space and uniqueness of a solution, and therefore to justify credibility of the decomposition procedure.

As the instrument measures only relative intensities (proportional to the number of detected photons), an important question arises; how to normalize the spectral intensities so that the experimental and calculated spectra could be compared when evaluating the difference function (4.3)? One possibility is to require the areas under curve of the two spectra to be equal. This is restated mathematically in (4.4).

Find N such, that $\qquad$ (4.4a)

$$N \int_{\omega_{\min}}^{\omega_{\max}} d\omega \, |S_{\exp}^{\text{inst}}(\omega)| = \int_{\omega_{\min}}^{\omega_{\max}} d\omega \sum_i c_i |S_i(\omega')|. \qquad \text{(4.4b)}$$

Then set $S_{\exp} = N S_{\exp}^{\text{inst}}$. $\qquad$ (4.4c)

$S_{\exp}^{\text{inst}}$ is the experimental spectrum in instrumental units and $S_{\exp}$ is then the normalized spectrum to be used in decomposition, absolute values are used for the case of ROA spectra which possess both positive and negative intensities. The ω' on the right-hand side of (4.4b) is a reminder that caclulated frequencies are scaled (4.2). Since the normalization condition (4.4b) requires knowledge of the coefficients $\{c_i\}$ obtained by minimization of the difference function (4.3), which in turn requires normalization, the process is done iteratively.

1. Set all coefficients $c_1, c_2, \ldots, c_n$ to $1/n$ (or any other initial values).

2. Normalize the experimental spectrum by satisfying the normalization condition (4.4).

3. Find a new set of coefficients $\{c_i\}$ that minimize the difference function (4.3) while satisfying conditions (4.1b).

4. Repeat steps 2 and 3 until values have converged.

Physically it is meaningful to normalize both the Raman and ROA spectra by the same constant, because their ratio should be independent of units. Raman spectra appear to be the stronger candidate for the search of a common normalization constant because they are measured to a much higher accuracy than ROA and spectral curves do not vary as significantly from conformer to conformer. In fact, the total Raman intensity should be conformer invariant according to the Raman intensity sum rule [Polavarapu, 1982].

It may, however, occur that the Raman spectrum is burdened by a fluorescence background which artificially increases the total spectral intensity. Commonly used attempts to correct for the fluorescence background by subtracting a fitted polynomial do not solve this problem rigorously. In these cases, the physical arguments may become unreasonable and performing a normalization independently for Raman and ROA spectra may be the better option.

A third possibility would be not to consider the normalization condition (4.4) at all. This would account to minimizing the difference function (4.3) without imposing the condition $\sum_i c_i = 1$. Only when the result is obtained would the coefficients be normalized to give them meaning, e.g. the result $(c_1, c_2, c_3) = (156, 793, 351)$ would be interpreted as $(12\,\%, 61\,\%, 27\,\%)$.

All three above mentioned approaches to spectral decomposition were tested. That is:

(d-a) Normalize the Raman experimental spectrum so to satisfy (4.4), normalize the ROA experimental spectrum using the same constant.

(d-b) Find an appropriate normalization constant for Raman and ROA spectra independently.

(d-c) Do not impose the normalizaiton condition (4.4), minimize δ (4.3) without imposing $\sum_i c_i = 1$. Normalize coefficients at the end to give them meaning of conformer population ratios.

4.3 Results and Discussion

Torsional angles determining dialanine conformation were defined in agreement with the standard ψ, ω, φ notation. The two distinct ψ angles were labelled ψ_N and ψ_C with respect to whether the angle is closer to the N- or C-terminus. The definition of torsional angles is depicted in figure 4.5.
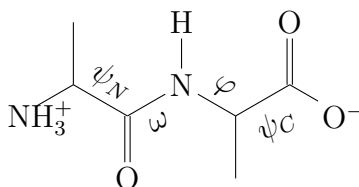
Figure 4.5: Definition of torsional angles (zwitterionic dialanine). Note that the four atoms needed to define a torsional angle unambiguously were chosen along the peptide backbone, that is along the "horizontal" direction in the figure.

4.3.1 Conformational Changes Induced by pH.

From an unconstrained MD histogram analysis of the backbone torsional angles we came to conclude that the φ and ψ_N angles are most important for molecular conformation, the other angles oscillate around a single value. Histograms of angle occurrences are plotted in appendix A (page 53).

On the basis of free-energy profiles (potentials of mean force) dependent on φ and ψ_N as obtained from the free- and WHAM-MD analyses we identified four principal conformers (A, B, C, D) for each of the protonated, zwitterionic and deprotonated forms of dialanine. Two other conformers (E, F) were also examined, but both their Boltzmann contribution according to MD and their weights obtained from decomposition were below 1 %, so these will not be discussed further. The results are presented in figure 4.6 (page 33), a table listing angles of considered minima on the (φ, ψ_N) potential energy surface is given in appendix B (page 55). The free-MD results agree well with those of WHAM-MD, indicating a relatively good equilibration of the most probable peptide conformers within the time of simulation (1 ns). In general, these results are consistent with previous MD studies, performed mostly on the zwitterionic form [Cornell et al., 1996, Wang et al., 2000, Foloppe and MacKerell Jr, 2000, Duan et al., 2003].
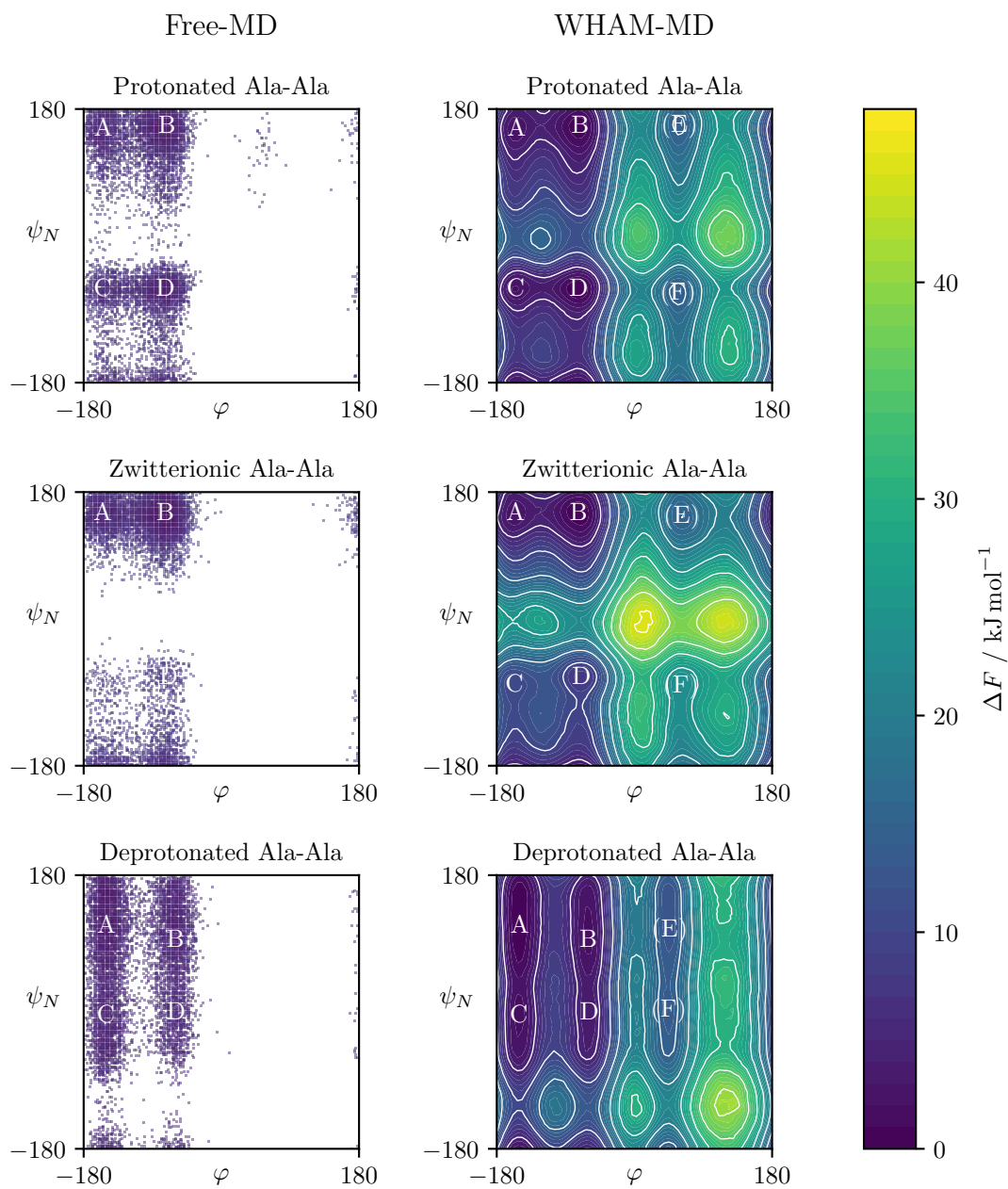
Figure 4.6: Ramachandran plots of the φ and ψ_N angles resulting from unconstrained (left) and WHAM (right) MD of d0-Ala-Ala. The effect of deuteration is negligible. Main conformers (A – D) are labeled as well as conformers E and F, although their Boltzmann populations and weights obtained from spectral decomposition were found to be negligible.

The zwitterion mostly adopts extended (A) and more puckered (B) conformations that would respectively correspond to β-sheet and polyproline II-like standard protein secondary structures [Creighton, 1993]. The polyproline II conformation is often identical to the so called random peptide conformation [Dukor and Keiderling, 1991]. In both the A and B forms the ψ_N angle is close to 152°, being stabilized by internal hydrogen bonding between the NH_3^+ group and amide oxygen. In the protonated form, ψ_N angles of about 57° proper to the C and D conformers appear more frequently. The D conformer is close to standard α-helix (or 3_{10}-helix), while C does not have a longer polypeptide analogue [Creighton, 1993]. The deprotonated high-pH form is more flexible in ψ_N than the other forms, i.e. the angle is predicted to move in wider intervals (see bottom of figure 4.6, page 33). Visualization of the four principal conformers can be found in appendix B on page 56.

We can therefore speak of changes in conformer equilibria. Although a dependence of dialanine conformation on pH has beed observed before, *ab initio* modeling of the potential energy surface did not provide satisfying results because of inadequate representation of the solvent [Jalkanen et al., 2003, Sychrovský et al., 2008, Knapp-Mohammady et al., 1999]. In particular, the dielectric polarizable continuum solvent models do not support well hydrogen bonding interactions and separation of charged molecular parts enabled by the polar aqueous environment [Bouř et al., 2005b, Buděšínský et al., 2008].

4.3.2 Spectral Decomposition

Firstly, the analytic properties of the difference function δ (4.3) were examined to obtain an understanding of its smoothness and uniqueness of minima. For both Raman and ROA spectra δ turned out to be perfectly smooth and possessed only a single minimum, as is illustrated in figure 4.7 (page 35). This result shows that the decomposition procedure is mathematically well defined and allows for improving the algorithm in which the minimum of δ is searched for. For example, instead of exploring the entire coefficient space by a small step size (say 0.01), one may begin searching in coarse steps and refine the result only in the vicinity of the best fit from the previous step. In our case this led to a speed up of the calculations from some 20 minutes to about 2 s.

Secondly, the three approaches to decomposition given as (d-a), (d-b) and (d-c) on page 32 were tested. The idea for judging their performance was that the d0-, d2- and d8-Ala-Ala forms should provide identical conformer ratios. Quantification of this criterion in the sample standard deviation sense within the series of three different samples (d0-, d2- and d8-Ala-Ala), each in three different forms (protonated, zwitterionic, deprotonated), is given in table 4.1 (page 35).

Comparing conformer ratios obtained by decomposing Raman and ROA spectra we see that ROA results are more stable, though in the case of (d-a) the performance is nearly identical. Normalizing ROA using the same constant as for Raman (d-a) spectra appears to disfavor decompositions from ROA spectra, but it also improves the agreement between Raman and ROA results, so on these grounds it remains speculative which approach is better.

Despite a comparable overall performance, individual results obtained from the different decomposition approaches varied significantly in some cases (largest
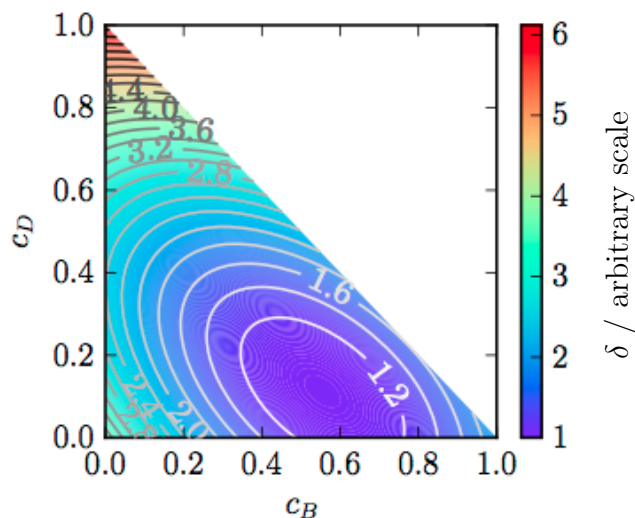
Figure 4.7: An example of a 2-D slice of the difference function δ (4.3) as dependent on two coefficients. The remaining coefficients were chosen to minimize δ. The situation regarding smoothness and uniqueness of a minimum was found to be qualitatively identical for all coefficients and for both Raman and ROA spectra.

Approach to Decomposition	Raman Spectra	ROA Spectra	Agreement Between Raman and ROA
(d-a)	9.4 %	9.3 %	6.9 %
(d-b)	9.4 %	6.7 %	8.9 %
(d-c)	9.7 %	6.4 %	7.6 %

Table 4.1: Quantification of various approaches to spectral decomposition (defined of page 32) in terms of sample standard deviation. Deviation was calculated from the average of d0-, d2- and d8-Ala-Ala coefficient results, as these should be equal.

differences between two coefficients were about 30 %). The "physical" approaches (d-a, d-b) seem to lead to better results for spectra uncorrupted by baseline or fluorescence problems, whereas the more "mathematical" approach (d-c) appears preferable when the experimental spectrum suffers from these issues, even when polynomial baseline corrections are used. However, this is not absolutely clear from our data.

Based on the slightly better performance (table 4.1, page 35) and a visual comparison of the resulting spectra (results not presented) we chose to work with approach (d-c) to weigh the conformer spectra in the following section.

4.3.3 Experimental and Calculated Spectra, Conformer Populations

The simulated spectra of conformers A – D along with their Boltzmann average, decomposition-weighed average and experimental spectra are depicted in figure 4.8 (page 37) for protonated d0-Ala-Ala. Similar graphs for all studied dialanine forms are found in appendix C, page 57. Looking at figure 4.8 (page 37), it is clear that the spectrum weight-averaged by the decomposition coefficients represents the experimental spectrum better than any individual conformer or the WHAM-MD weighed average[2], although occasional inconsistencies persist. For example, negative ROA bands at $850 \, \text{cm}^{-1}$, $1090 \, \text{cm}^{-1}$ and $1268 \, \text{cm}^{-1}$ corresponding to a delocalized vibration, hydrogen bending and an amide III mode respectively [Šebek et al., 2009] are not reproduced by the simulations. We verified that inclusion of other conformers (E, F) does not improve the results considerably. Therefore we attribute the remaining error of the simulations to intrinsic inaccuracies of the DFT harmonic force field [Prampolini et al., 2015], neglect of the anharmonic interactions [Daněček et al., 2007] and possibly also to an insufficient number of MD snapshots [Hopmann et al., 2011]. Vibrational frequencies are very sensitive to proper treatment of electron correlation [Cortez et al., 2007], currently only approximately included in DFT. Nevertheless, overall, the simulations do reproduce most of the features observed experimentally, both in the Raman and ROA spectra, and thus provide a good basis for the conformer analysis.

Coefficients of A – D conformer populations as obtained by the WHAM-MD / Boltzmann scheme and decomposition of Raman and ROA spectra are listed in table 4.2 (page 39). This data set is also represented graphically in figure 4.9 (page 38). Despite some variance in the coefficients obtained from decomposition, considerable deviations of conformer populations from the WHAM-MD can be seen. This is most notable in the case of protonated Ala-Ala, where the WHAM-MD populations of C (12 %) and D (35 %) appear unrealistically high given the nearly zero populations predicted from both Raman and ROA spectral analyses.

The Raman / ROA spectroscopy combined with spectral simulations could thus open a way to improve molecular dynamics force fields. Nevertheless, at this stage we do not consider our results to be of benchmark quality. A deeper analysis

---

[2]The example of protonated dialanine is chosen here because it best manifests the improvement of the decomposition over WHAM-MD averaging because the MD appears to have performed worst for the protonated form. The overall trend however, that the decomposition improves spectra notably, is a generally observed one (see appendix C, page 57).
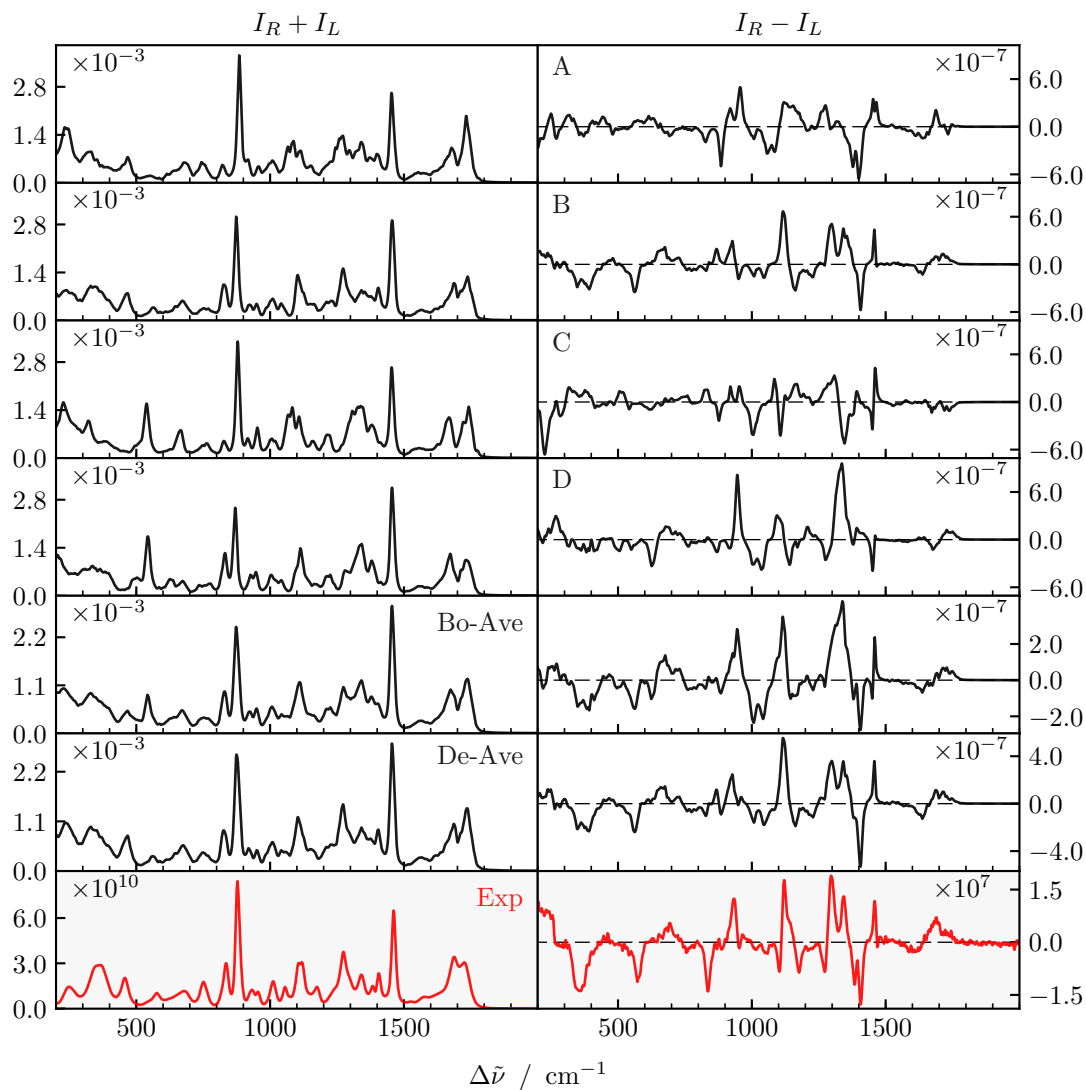
Figure 4.8: Protonated (undeuterated) dialanine spectra. Individual conformer (A – D), WHAM-MD / Boltzmann-averaged (Bo-Ave), averaged by coefficients obtained from spectral decomposition (De-Ave) and experimental (Exp.) spectra. Raman (left) and ROA (right). Calculated frequencies have been scaled according to equation (4.2). Intensity units are arbitrary for calculated spectra and experimental spectra are given in instrumental units.
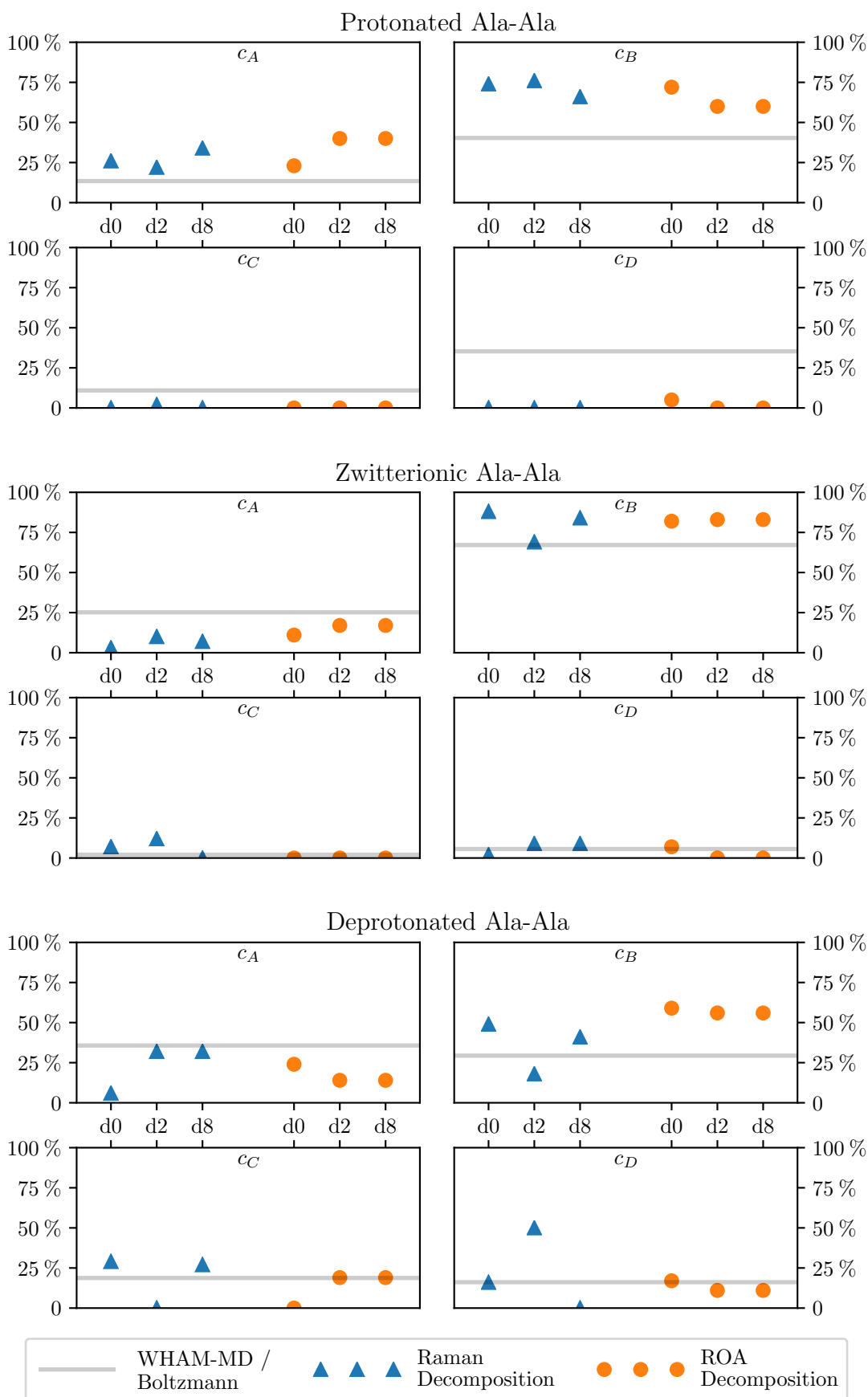
Figure 4.9: Graphical representation of data from table 4.2 (page 39); conformer coeficients as obtained from decomposition of Raman spectra, decomposition of ROA spectra and the WHAM-MD / Boltzmann scheme.

Ala-Ala Form[*]		WHAM-MD / Boltzmann Coefficients $(c_A, c_B, c_C, c_D)^\S$	Raman Decomposition Coefficients[†] $(c_A, c_B, c_C, c_D)^\S$	ROA Decomposition Coefficients[†] $(c_A, c_B, c_C, c_D)^\S$
P	d0	$(13, 40, 12, 35)$	$(26, 74, 00, 00)$	$(23, 72, 00, 05)$
	d2	—	$(22, 76, 02, 00)$	$(40, 60, 00, 00)$
	d8	—	$(34, 66, 00, 00)$	$(40, 60, 00, 00)$
Z	d0	$(25, 67, 02, 06)$	$(03, 88, 07, 02)$	$(11, 82, 00, 07)$
	d2	—	$(10, 69, 12, 09)$	$(17, 83, 00, 00)$
	d8	—	$(07, 84, 00, 09)$	$(17, 83, 00, 00)$
D	d0	$(36, 29, 19, 16)$	$(06, 49, 29, 16)$	$(24, 59, 00, 17)$
	d2	—	$(32, 18, 00, 50)$	$(14, 56, 19, 11)$
	d8	—	$(32, 41, 27, 00)$	$(14, 56, 19, 11)$

[*] P: Protonated, Z: Zwitterionic, D: Deprotonated.
[†] Using approach (d-c) defined in section 4.3.2.
[§] Given in %.

Table 4.2: Conformer coeficients as obtained from decomposition of Raman spectra, decomposition of ROA spectra and the WHAM-MD / Boltzmann scheme.

of inconsistencies between the MD calculated and experimental conformer ratios would have to consider the approximations used in the Amber03 force field, which is optimized to represent helix-coil peptide transitions well [Best and Hummer, 2009], and the TIP3P64 water force field (part of Amber03).

4.4   Author Contributions, Acknowledgements

Molecular dynamics and *ab initio* calculations were performed by the thesis author. The thesis author also coded the software for spectral decomposition (SpeDec, a Python package of scripts) which is already being used by other members of the group. Synthesis of deuterated dialanines was done by Jaroslav Šebestík and Martin Šafařík. Experimental spectra were acquired by Josef Kapitán, Jaroslav Šebestík and the thesis author. The entire project was supervised by Petr Bouř.

The author is indebted to Jiří Kessler for an introduction to many of the computational chemistry methods used. Jana Hudecová is acknowledged for independently testing the SpeDec software in early stages of development.

5. ROA Measurement of Lysozyme Amyloid Fibrils

Many proteins assemble into fibrillar (long and narrow) shapes which have specific structural or motility roles in living organisms (e.g. collagens, elastins, myosin). What sets amyloids apart is their often abnormal size and, more importantly, their association with pathological processes, many of which are neurodegenerative in character (Alzheimer's, Parkison's, Creutzfeldt-Jakob's, mad-cow disease).

An important characteristic of amyloids is their stability, which on one hand complicates the aspiration to reverse the process of their formation in tissues of living organisms, on the other hand it makes them interesting as potentially useful structural units in bionanotechnology. For these reasons amyloids have gained significant attention in the past few decades, yet many questions about the mechanism of their formation and their structure remain unanswered.

Raman optical activity (ROA) could provide valuable insight into amyloid fibril morphology, as it can give this information about the principal building blocks of amyloids; peptides (chapter 4) and proteins [Kessler et al., 2015]. Previously there have also been successful ROA studies of pre-fibrillar intermediates [Blanch et al., 2000]. However, the inhomogeneous nature of fibrillar samples makes their measurement quite challenging. To our knowledge, ROA measurement of an amyloid has been reported only once, specifically of insulin fibrils [Yamamoto and Watarai, 2012]. Experimental data would be especially valuable to our group as theoretical models for fibrillar samples are already in development.

In this chapter we present the progress we have made in attempting ROA measurement of such samples. We chose to begin with (hen egg white) lysozyme because it is an extensively studied protein with plenty of literature on fibril preparation available. That being said, lysozyme fibrils are not exclusively of academic interest, they are associated with the hereditary nonneuropathic systemic amyloidosis disease [Rambaran and Serpell, 2008].

5.1 Preliminaries

Amyloid fibril properties. Amyloids organize into net-like structures (see figure 5.1a, page 42) which macroscopically result in a clear of slightly milky, insoluble gel-like form[1]. X-ray studies have revealed that the principal binding force in amyloids is non-covalent bonding between β-strands, which are oriented perpendicular to the fibril axis (figure 5.1b, page 42), resulting in a cross-β structure [Makin et al., 2006].

From an optical point of view, an important aspect of these aggregates is that they exhibit birefringence [Missmahl and Hartwig, 1953]. This greatly complicates chiroptical measurements where preserving light polarization before and

---

[1]It is perhaps interesting to note that the term *amyloid* was introduced in 1854 when Rudolf Virchow came to conclude that the macroscopically abnormal thick gel he found in cerebral tissue was starch (*amylum* in Latin). Even though the claim was disproved only five years later when the protein nature was correctly ascribed by Freidreich and Kekule, the name amyloid has remained [Sipe and Cohen, 2000].
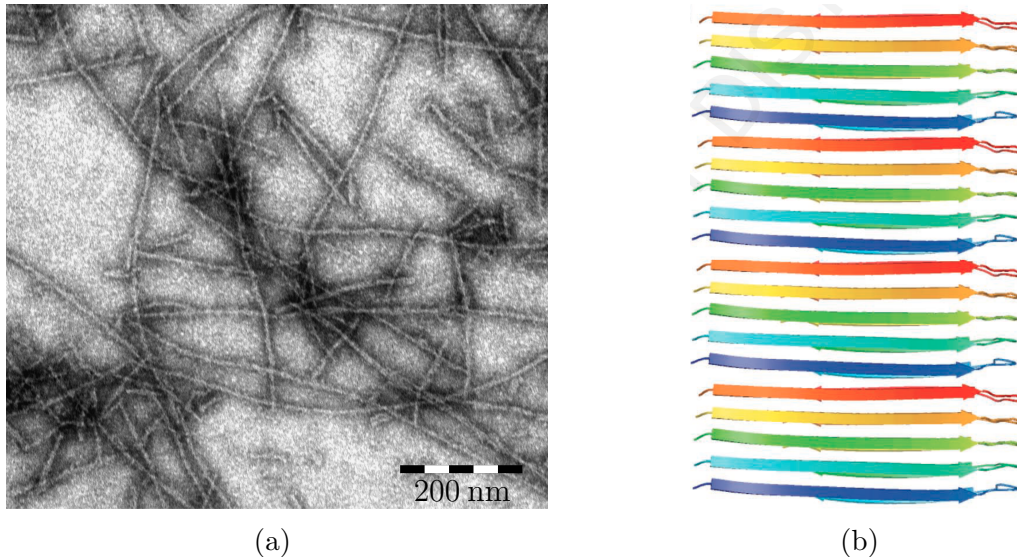
(a)   (b)

Figure 5.1: Amyloid fibril structure. (a) Transmision electron microscope image of (hen egg white) lysozyme fibrils. (b) Cross-β structure typical for amyloids, the β-strands run perpendicular to the fiber axis (from [Rambaran and Serpell, 2008]).

after the absorption or scattering events is crucial, but both electronic and vibrational circular dichroism approaches appear feasible for fibrils [Barrow et al., 1992, Ma et al., 2007] and ROA of an amyloid has been reported once as well [Yamamoto and Watarai, 2012].

Amyloid fibril formation. In a combined X-ray, Fourier-transform infrared spectroscopy and electronic circular dichroism study, Booth et al. [1997] have proposed a molecular mechanism for lysozyme fibril formation. We present it here in figure 5.2 (page 43). From similarities in the structure of various fibrils, this mechanism is thought to be rather universal, not specific for lysozyme.

The key step in (the proposed and widely accepted) fibrillogenesis is partial unfolding of native protein. This can be induced thermally or chemically by changing pH or addition of denaturing agents such as ethanol. Once these partly unfolded molecules begin to aggregate, it is thought that their hydrophobic regions become exposed, solubility decreases and the aggregation process is accelerated. The intermediate states thus act as "seeds" in a crystallization-like mechanism [Come et al., 1993]. Treatment of forming fibrils with ultrasound can lead to their fragmentation resulting in higher seed concentrations. Consequently, faster kinetics and a higher protein to fibril transformation ratio may occur [Stathopulos et al., 2004].

The presence of fibrils can be conveniently detected by fluorescence measurements of the sample with the addition of thioflavine T. This dye selectively binds to fibrillar structures and if this occurs, an increase in fluorescence by several orders of magnitude can be observed [LeVine, 1995].

Experimental intentions. In approaching the problem of measuring these inhomogeneous samples, two strategies were intended. Firstly, an all new round, rotating cuvette (depicted in figure 5.3b, page 44) would be tested. We anticipated that false signals stemming from the inhomogeneous nature of samples could be averaged out by the rotation. Constant mixing of insoluble samples
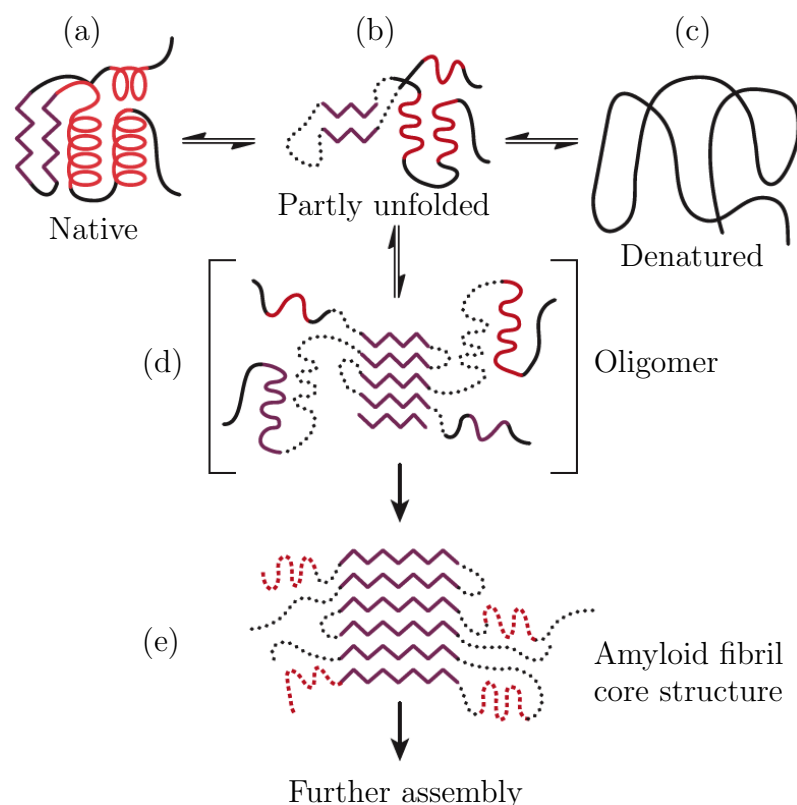
Figure 5.2: Proposed mechanism for lysozyme fibril formation. A partly unfolded (molten globule) form of the protein (b), distinct from the native (a) and denatured (c) forms, associates through the β-domain initiating oligomer formation (d). This provides a template for the further deposition of protein and for the development of the stable, mainly β-sheet, core structure of the amyloid fibril (e). Purple: β-sheet, red: helical structure, black: random coil, dotted lines: undefined structure. Mechanism proposed by Booth et al. [1997], picture adapted from [Selkoe, 2003].

should also help keep the desired molecules within the path of the laser beam, as these may otherwise sediment, self-aggregate etc.

Secondly, measurement in different polarization modes would be attempted,[2] as this is fairly uncharted territory. Contemporarily, the only commercially available ROA spectrometer (BioTools) operates in the SCP arrangement. A recent report, in which the BioTools instrument was extended to all polarization modes (ICP, SCP, DCP_I, DCP_{II}) and ROA of α-pinene and lysozyme solution were measured, came to conclude that the DCP_I mode is superior to ICP and SCP in terms of minimal parent Raman intensity resulting in a favorable signal-to-noise ratio, a reduced susceptibility to artefacts and a reduced Rayleigh background intensity [Li and Nafie, 2012]. The only previous ROA measurement of an amyloid was done on a home-built ICP spectrometer [Yamamoto and Watarai, 2010, 2012].

---

[2]For a definition of polarization modes in ROA, see section 2.3, page 14.

(a) Standard cuvette,
$V \approx 100\,\mu l$

(b) Rotational cuvette,
$V \approx 1\,ml$

(c) Slow rotation,
$\nu \approx 0.1\,Hz$

(d) Fast rotation,
$\nu \approx 50\,Hz$
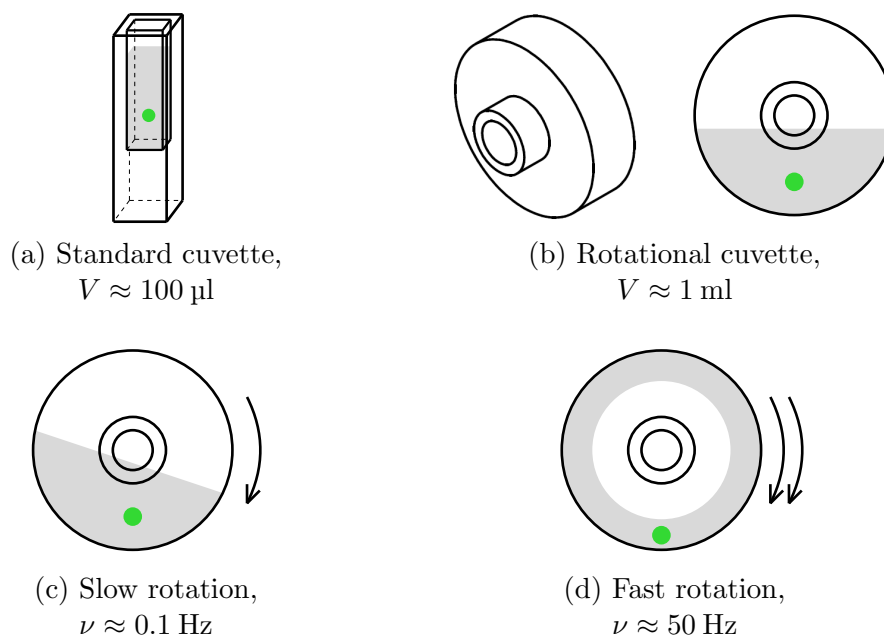
Figure 5.3: ROA fused silica cuvettes. Types and volumes (a, b) and two modes of rotational cuvette operation (c, d). Gray (▢) signifies the sample, the green dot (●) depicts where the laser beam enters the cuvette.

5.2 Results

5.2.1 Lysozyme Fibril Preparation Protocol

The first task was to prepare fibril samples. Even though the literature on lysozyme fibril preparation *in vitro* is quite abundant, most studies work with $\sim 1\,mg\,ml^{-1}$ concentrations, vibrational spectroscopies typically require concentrations in the range $50 - 100\,mg\,ml^{-1}$ for signals to be detectable. The only protocol we found for lysozyme fibrils at such high concentrations was that of Ma et al. [2007]. Their instructions were

1. Prepare a $100\,mg\,ml^{-1}$ solution of hen egg white lysozyme, acidify to pH 2,

2. Incubate at $65\,°C$ for $48\,h$,

3. Separate fibrils from solution by centrifugation.

Unfortunately, this procedure gave rather irreproducible results (sometimes fibrils formed, sometimes not) and even when fibrils formed, the yield was usually very low. By further consulting literature (most notably [Arnaudov and de Vries, 2005] and [Stathopulos et al., 2004]), consulting with other groups at the Institute and some trial and error, we arrived at a more effective protocol.

1. Prepare a $100\,mg\,ml^{-1}$ solution of hen egg white lysozyme, acidify to pH $1.6 - 2$.[3,4]

---

[3]Working with pH 1.6 results in white flakes appearing in the formed gel more often than when working with pH 2. It is unclear to us whether these flakes are also fibrils or some aggregate without supramolecular structure. However, when mature fibrils do appear in the form of a clear gel, working with pH 1.6 seems to give a higher yield.

[4]Some sources recommend preparing fibrils at a pH near the isoelectric point, as charged

44

2. Incubate at 60 °C for 24 h.

3. Sonicate in an ultrasonic bath for 1 h.

4. Repeat incubation at 60 °C for 24 h.

5. Repeat sonication in an ultrasonic bath for 1 h.

6. Repeat incubation at 60 °C for 24 h.

7. Convert formed gel into viscous liquid (necessary for the centrifugation in step 8 to be effective). Sometimes this can be achieved using a vortex mixer. Sonication for 20 minutes or freezing the sample are more effective methods, although it is possible that the sample will suffer damage from these.

8. Separate fibrils from solution by centrifugation (20 minutes at 14000 rpm). The fibrils sediment and the supernatant may be poured out.

9. Test presence of fibrils by a thioflavine T fluorescence measurement.

The result of this preparation process is usually a clear viscous liquid that cannot be measured directly, because the viscosity does not allow bubbles to escape or for the sample to be mixed in the rotational cuvette. Our solution was to resuspend the sample in water with pH adjusted to that of the original sample, usually addition of water in a 1 : 1 ratio to the sedimented sample was sufficient for the sample to be handled further.

5.2.2 Rotational Cuvette Performance

Rotation speed. Firstly, different rotation speeds of the round cuvette were tested, see figures 5.3c and 5.3d (page 44). For water there seemed to be no difference between the two speeds or a stationary setup. As for fibrils, at first fast rotation (~ 50 Hz) seemed to be better, because this allowed for more viscous (hence more concentrated) samples to be measured. The liquid would adhere to the sides and the bubbles escaped outside the laser beam to the center of the cell. However, after some hours of spectra acquisition it began to seem that slow rotation (~ 0.1 Hz) would be a better choice, as signals were generally a bit stronger and a bit less burdened with baseline drifts. The reason for this could be that during fast rotation, the fibrils concentrate near the edges of the cuvette where the laser cannot be focused. Therefore only slow rotation was used in following experiments.

Fluorescence background. A disadvantage of rotating the cuvette during measurement we observed was that a much higher fluorescence background appears than in a stationary setup. The reason for this is the higher sample volume and constant mixing preventing the fluorescing impurities to be disintegrated in the laser beam.

This problem could be partly circumvented using higher laser power. From our experience, the maximum laser power that fibrillar protein samples resist

---

molecules may repel each other. This was also tested, but hen egg white lysozyme precipitated around pH 9, that is before reaching its isoelectric point of pH 11.35 [Wetter and Deutsch, 1951].
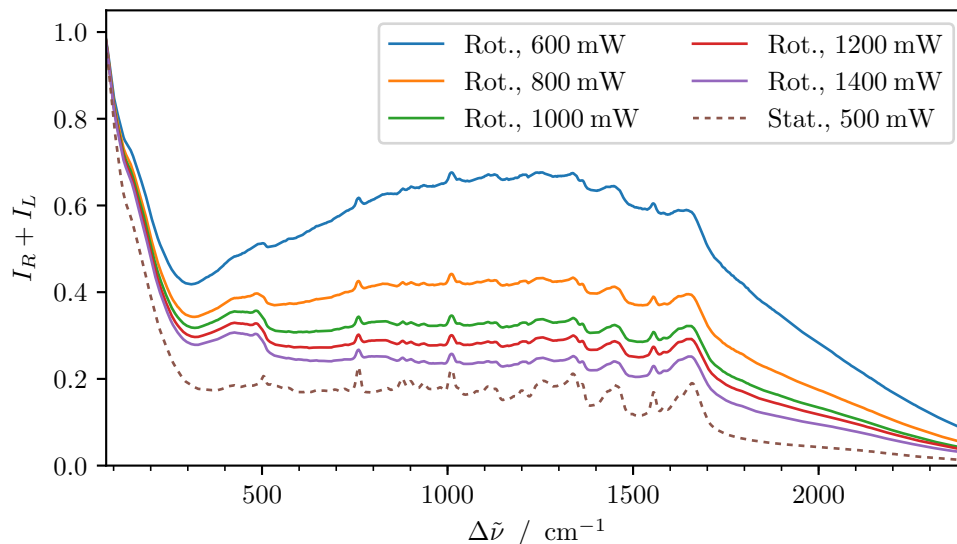
Figure 5.4: Raman spectra of lysozyme fibrils. Full lines represent consecutive 4h measurements on the same sample in a slowly rotating cuvette (0.1 Hz). The order of measurements was from lowest to highest laser power and the fluorescence background decreases respectively. Laser (532 nm) power is listed at source, the power reaching the sample was always very close to one half. The dashed line shows a measurement acquired within minutes in a stationary cell. All measurements were done using the BioTools instrument in the SCP arrangement. All spectra are plotted without any baseline or detector sensitivity correction, and normalized to the exact measurement time. Intensity units are arbitrary.

before burning in a standard cuvette is around 700 mW (about 350 mW at the sample). If the sample is being rotated, we found the sample to withstand double that for many hours, see figure 5.4 (page 46). Using a high laser power however considerably heats up the sample, which can lead to undesired consequences. For example, aggregation may be reinitiated and the liquid can turn back into a thick, unmeasurable gel.

Another possibility would be to photobleach the sample for many hours before measurement, but again the sample may be damaged by this. Filtration with syringe filters (0.2 μm pores, RC membrane) before incubation to remove impurities did not bring any improvement. The possibility to try ROA at a different wavelength would require construction of an entirely new spectrometer, a rather expensive project for many years.

Rotational cuvette summary. During the course of measurement we found only one advantage of the rotational cuvette and that was the immunity to sample sedimentation. The higher noise and baseline drift problems probably arise from the higher fluorescence background in the measured signal.

No sign of advantageous averaging over sample orientations has been recorded. The reason for this can be that any advantage is hampered by the higher fluorescence. Or it could be that the birefringence of samples is too high to be effectively eliminated by this averaging. The typical ROA / Raman signal intensity ratio is only $\sim 10^{-4}$ and a difference in the index of refraction for two orthogonal di-

rections in comparable or higher orders could completely annul the ROA signal. Another explanation could possibly be that the focal volume is already much larger than any characteristic length of fibrils. The length of a hypothetical focal cube is roughly $100\,\mu m$, $\sim 10^3$ times larger than the typical fibril length of $\sim 200\,nm$ (figure 5.1a, page 42). Thus possibly already in a standard cuvette an effective averaging over all possible sample orientations may be achieved.

5.2.3 Polariaztion Modes

Measurements using different polarization modes were performed at Palacký University in Olomouc, where a new ROA spectrometer has recently been built. The result of one such measurement is plotted in figure 5.5. It needs to be stressed that this measurement was made only once. Tests of reproducibility have not been successful so far due to deterioration of samples before or during measurement.
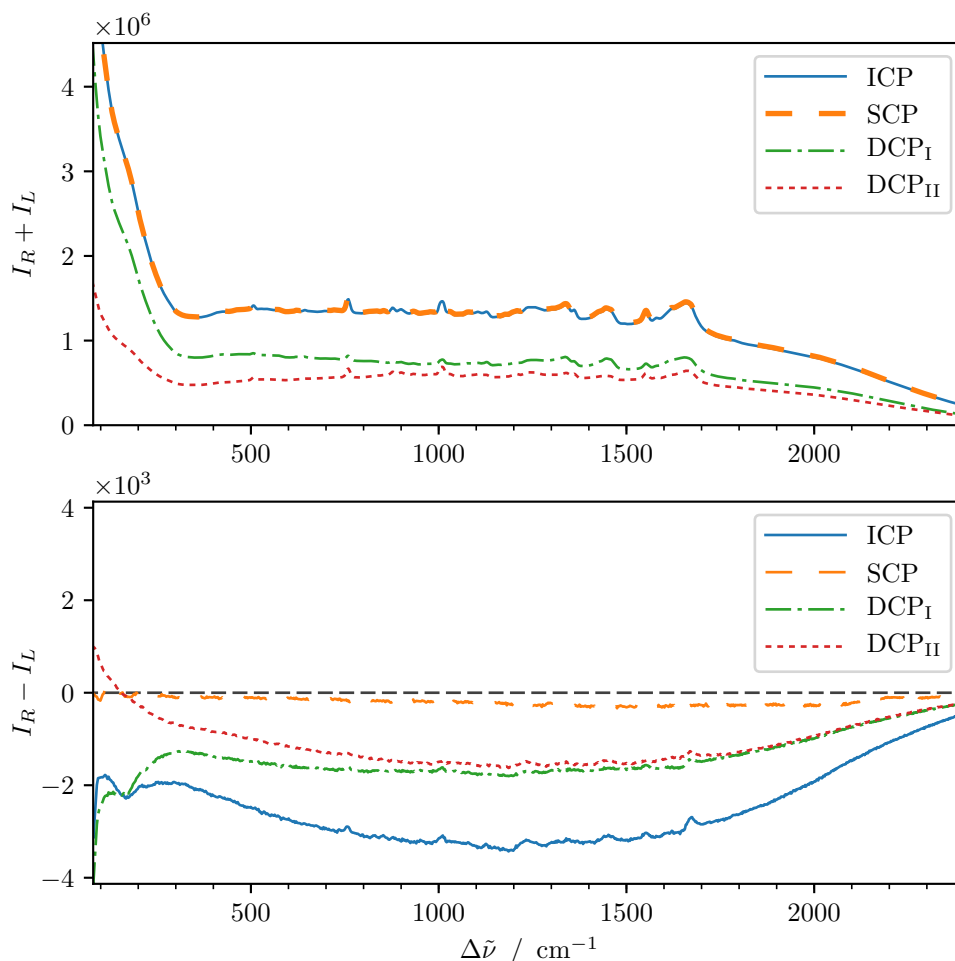
Figure 5.5: Raman (top) and ROA (bottom) spectra of lysozyme fibrils using various (simultaneously acquired) polarization modes and a slowly rotating cuvette (0.1 Hz). Laser (532 nm) power was 1000 mW at source, 730 mW at sample. Measured using a home-built ROA spectrometer at Palacký University. All spectra are plotted without any baseline or detector sensitivity correction. Intensity is given in instrumental units.

The Raman signal behaves exactly as would be expected, ICP and SCP give practically identical results and $DCP_I + DCP_{II}$ is equal to the previous two. In ROA the situation is not quite so clear. The SCP mode gives practically zero signal, the others show signs of a possible signal, but suffer strongly from baseline drifts. We interpret the zero SCP to be a result of sample birefringence annulling the ROA signal and the other modes to be more prone to detecting false signals. These false signals may originate in fluorescence of impurities, from the birefringence, from spectrometer design or other, unknown sources. SCP ROA measurements on the BioTools instrument most commonly resemble those of ICP in figure 2.3 (page 14).

Despite the efforts made, obtaining faithful and reproducible lysozyme fibril ROA has not been achieved so far.

5.3 Author Contributions, Acknowledgements

Conclusion

This thesis has presented an overview of Raman optical activity (ROA) areas of application and introduced basic biochemical concepts relevant to protein structure (chapter 1). In chapters 2 and 3, experimental and theoretical aspects of ROA were presented.

Chapter 4 contained an ROA study of the dipeptide dialanine, which has been studied multiple times by ROA before as a "minimal" peptide model. In comparison to previous works, a combined QM/MM approach was used for spectral simulations to account for multiple conformers of the studied molecule and the surrounding water solvent environment. It was clearly shown that the spectrum of any individual conformer is not sufficient, but when these spectra were weight-averaged, an unprecedented agreement between the experimental and simulated spectra resulted (figure 4.8, page 37, or appendix C). To obtain coefficients for the weight-averaging, two approaches were tested. One was based on a molecular dynamics (WHAM-MD) population analysis, the other was a mathematical decomposition of the experimental spectrum into individual conformer spectra. The decomposition procedure lead to considerable improvements in predicted spectra, and in some cases it was able to faithfully disprove conformer coefficients obtained the the WHAM-MD analysis. As the decomposition approach is not a well established technique, its mathematical properties (smoothness of the coefficient space and uniqueness of a solution) were examined with results being positive. Consistency of the decomposition results was tested on the set of three types of dialanine varying in deuteration levels, times three different forms according to pH. On this data set, the sample standard deviations for the coefficients were $9.7\,\%$ and $6.7\,\%$ for Raman and ROA spectra respectively. ROA spectra have therefore shown to be more stable in giving information on conformer populations.

Chapter 5 presented pioneering attempts to acquire ROA of lysozyme amyloid fibrils, difficulty of which stems from the inhomogeneous nature of fibrillar samples (insolubility, birefringence). Already preparation and handling of these samples at concentrations needed for vibrational spectroscopy ($\sim 100\,\mathrm{mg\,mol^{-1}}$) was challenging. Some progress towards a high protein to fibril transformation ratio and preparation reproducibility (difficult for amyloid fibrils in general) was made. As for the ROA measurements, an all new rotational sample cuvette was tested with the anticipation it could lead to an effective averaging out of false signals originating in the inhomogeneous nature of the samples. It proved to be advantageous in that the fibrils did not sediment, which can occur in a standard cuvette for insoluble samples. On the other hand, large issues with fluorescence arose when the sample was being rotated and these could be only partly overcome using higher laser powers (figure 5.4, page 46) than would be possible in a static cuvette due to local sample overheating. Various ROA polarization modes were examined and preliminary results suggest that the scattered circular polarization (SCP) mode is least prone to false signals and baseline drifts (figure 5.5, page 47).

Appendices

A. Ala-Ala: Molecular Dynamics Angle Histograms
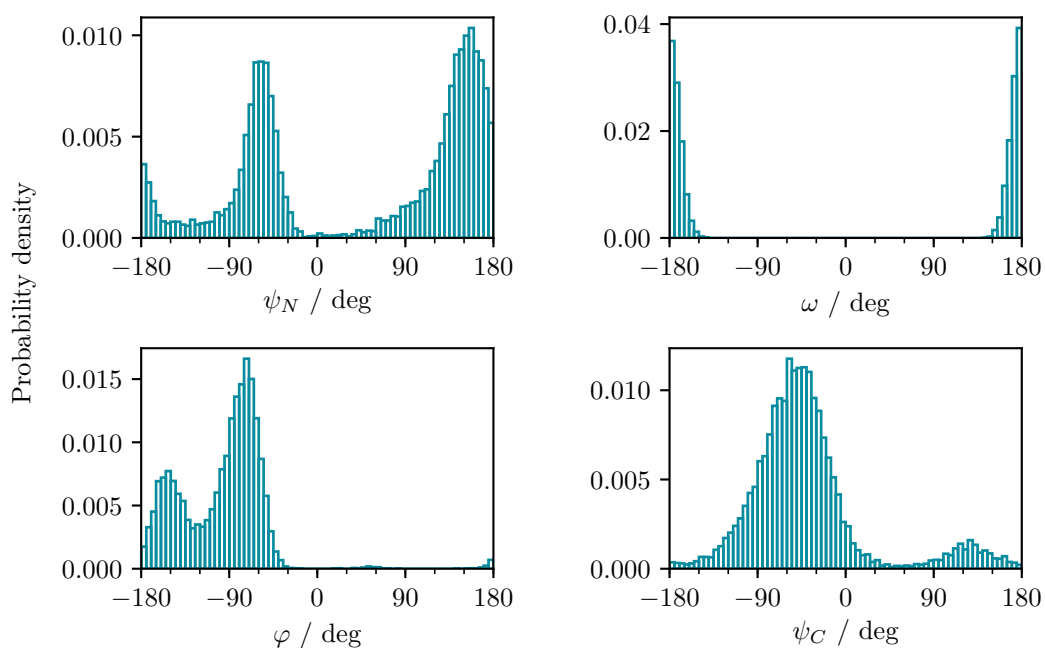
List of Figures

Figures

Figure A.1: Protonated d0-Ala-Ala torsion angle histograms obtained from unconstrained MD. The ψ_C population in the vicinity of 130° was not considered.
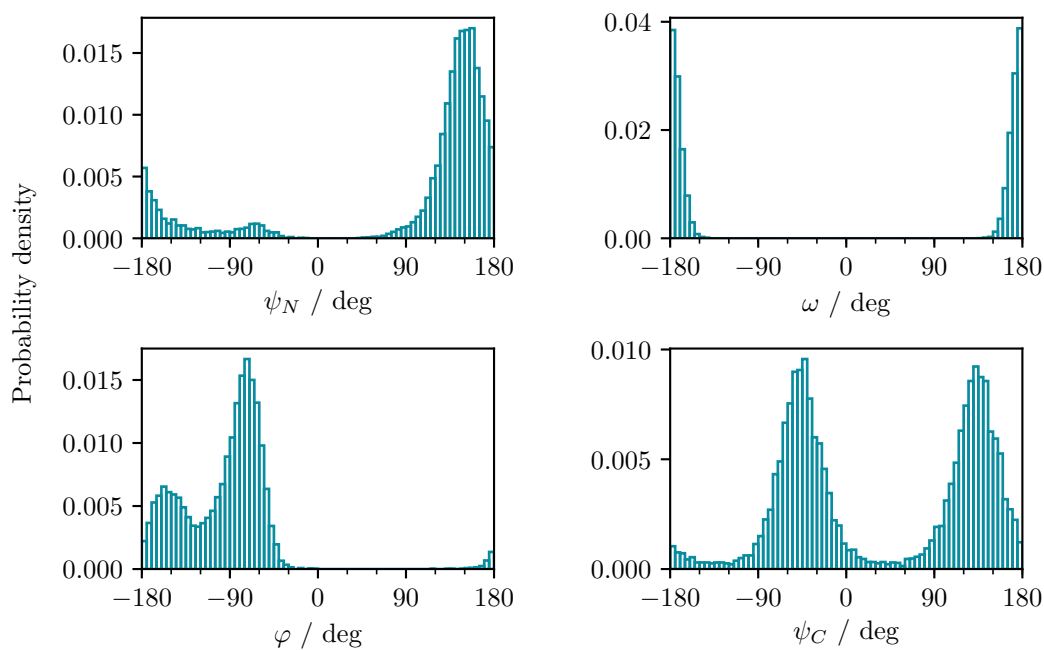
Figure A.2: Zwitterionic d0-Ala-Ala torsion angle histograms obtained from unconstrained MD. Note that the molecule is symmetrical under 180° rotation of ψ_C.
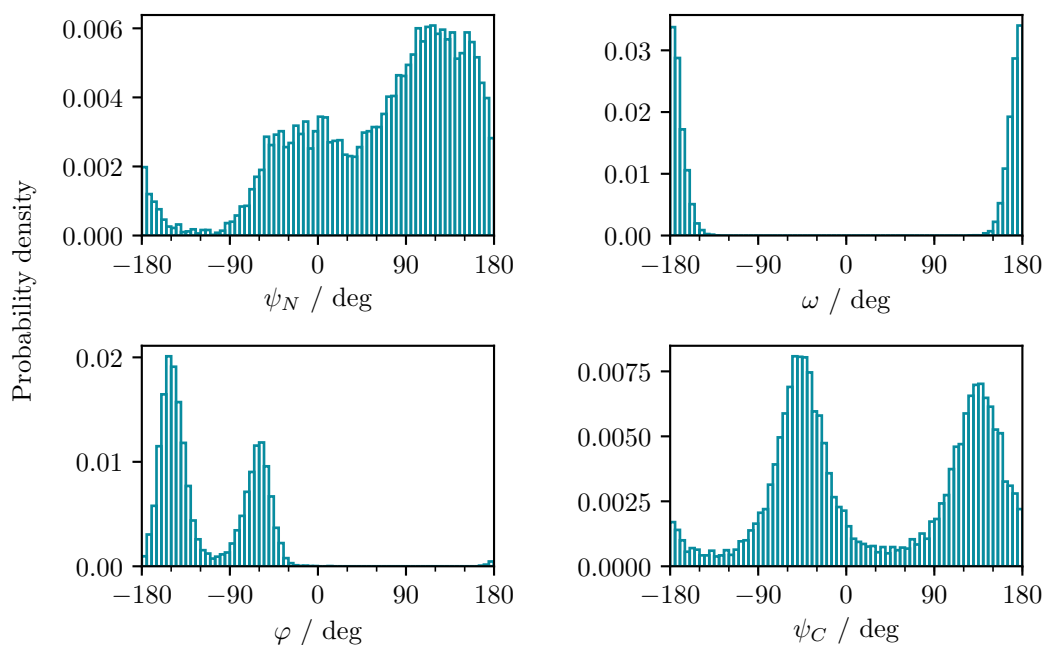

Figure A.3: Deprotonated d0-Ala-Ala torsion angle histograms obtained from unconstrained MD. Note that the molecule is symmetrical under 180° rotation of ψ_C.

B. Ala-Ala: List of Conformer Torsional Angles, Conformer Visualizations

Ala-Ala Form	Conformer	φ	ψ_N
Protonated	A	$-154°$	$153°$
	B	$-71°$	$157°$
	C	$-155°$	$-57°$
	D	$-73°$	$-58°$
	(E)	$59°$	$158°$
	(F)	$57°$	$-62°$
Zwitterionic	A	$-155°$	$152°$
	B	$-73°$	$152°$
	C	$-157°$	$-74°$
	D	$-69°$	$-64°$
	(E)	$62°$	$148°$
	(F)	$61°$	$-75°$
Deprotonated	A	$-150°$	$113°$
	B	$-60°$	$94°$
	C	$-151°$	$-5°$
	D	$-59°$	$-1°$
	(E)	$46°$	$107°$
	(F)	$45°$	$2°$

Table B.1: Ala-Ala conformer torsional angles (φ, ψ_N) as obtained from the WHAM-MD analysis.
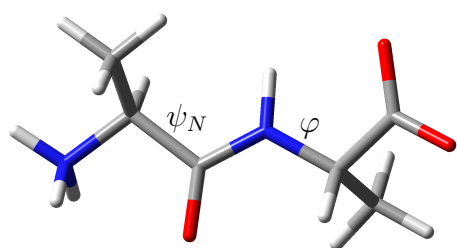
Conformer A
"β-sheet"
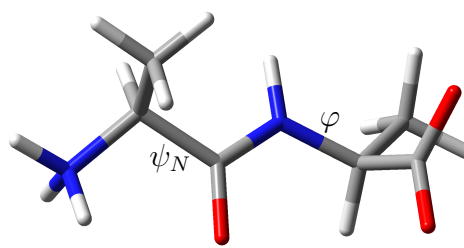
Conformer B
"Polyproline II"
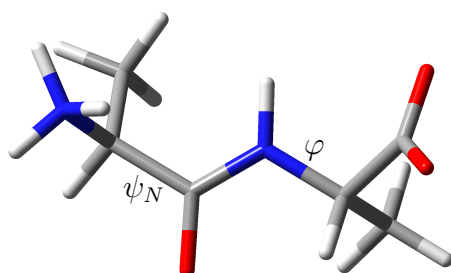
Conformer C
No polypeptide analogue
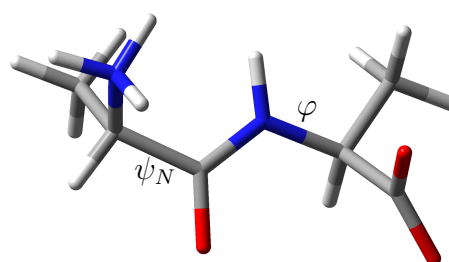
Conformer D
"α-helix"

Figure B.1: Principal conformers, depicted for zwitterionic dialanine.

C. Ala-Ala: Conformer, Boltzmann-Averaged, Decomposition-Averaged and Experimental Spectra

List of Figures

Figures

Caption common to all figures in this section. Individual conformer (A – D), WHAM-MD / Boltzmann-averaged (Bo-Ave), averaged by coefficients obtained from spectral decomposition (De-Ave) and experimental (Exp.) spectra. Raman (left) and ROA (right). Calculated frequencies have been rescaled according to equation (4.2). Intensity units are arbitrary for calculated spectra and experimental spectra are given in instrumental units.
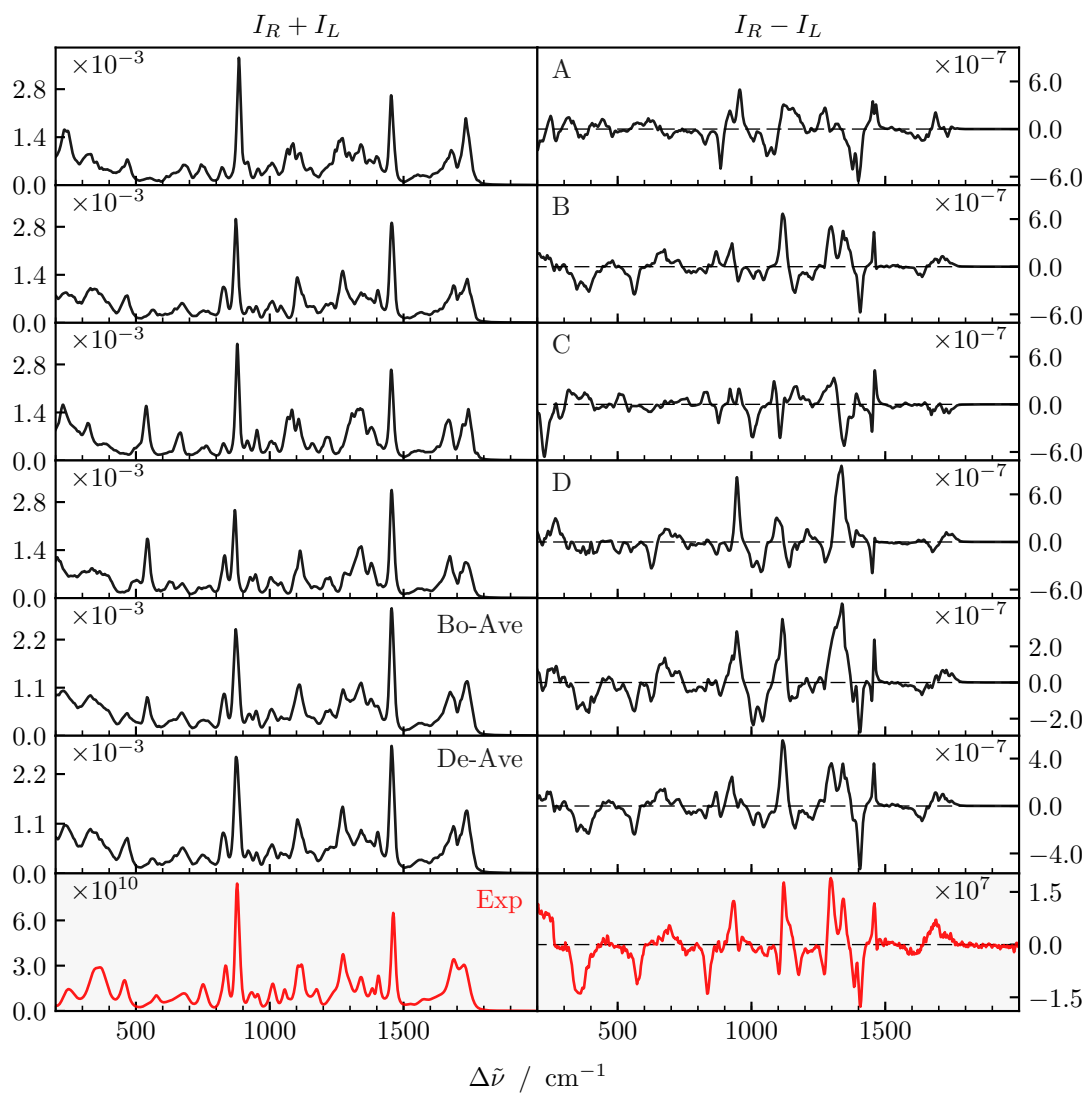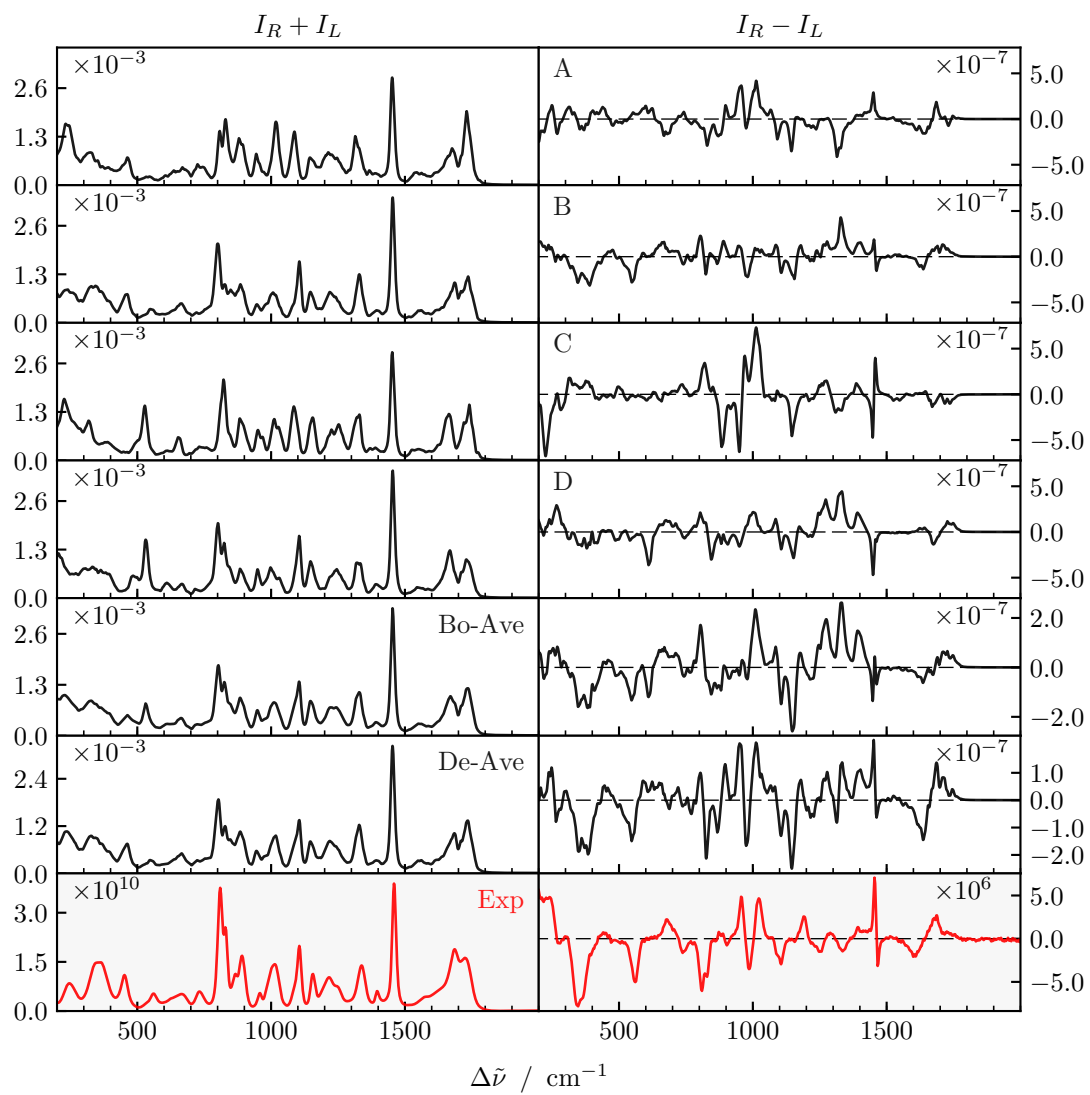
Figure C.1: Protonated d0-Ala-Ala spectra.

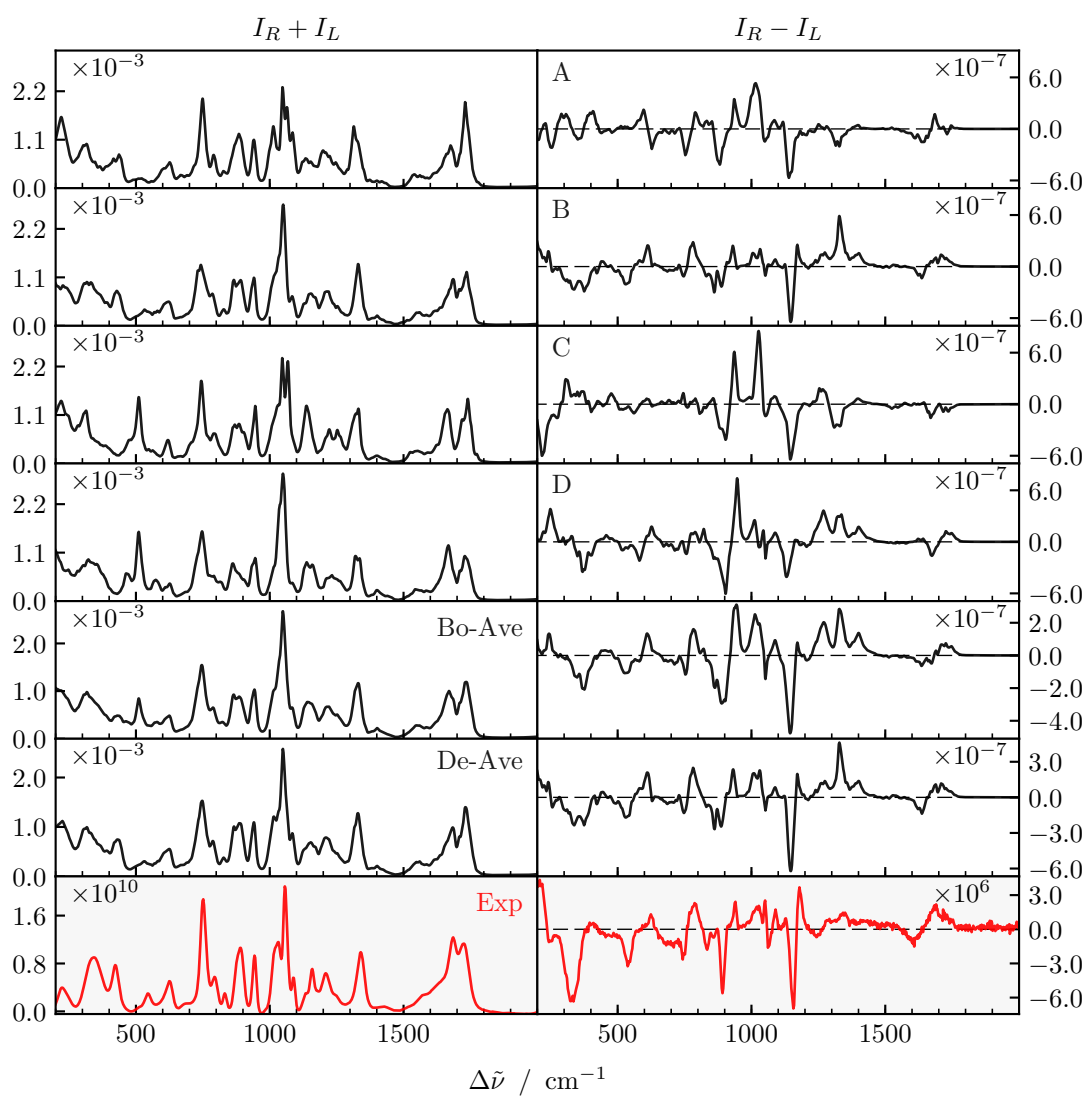Figure C.2: Protonated d2-Ala-Ala spectra.

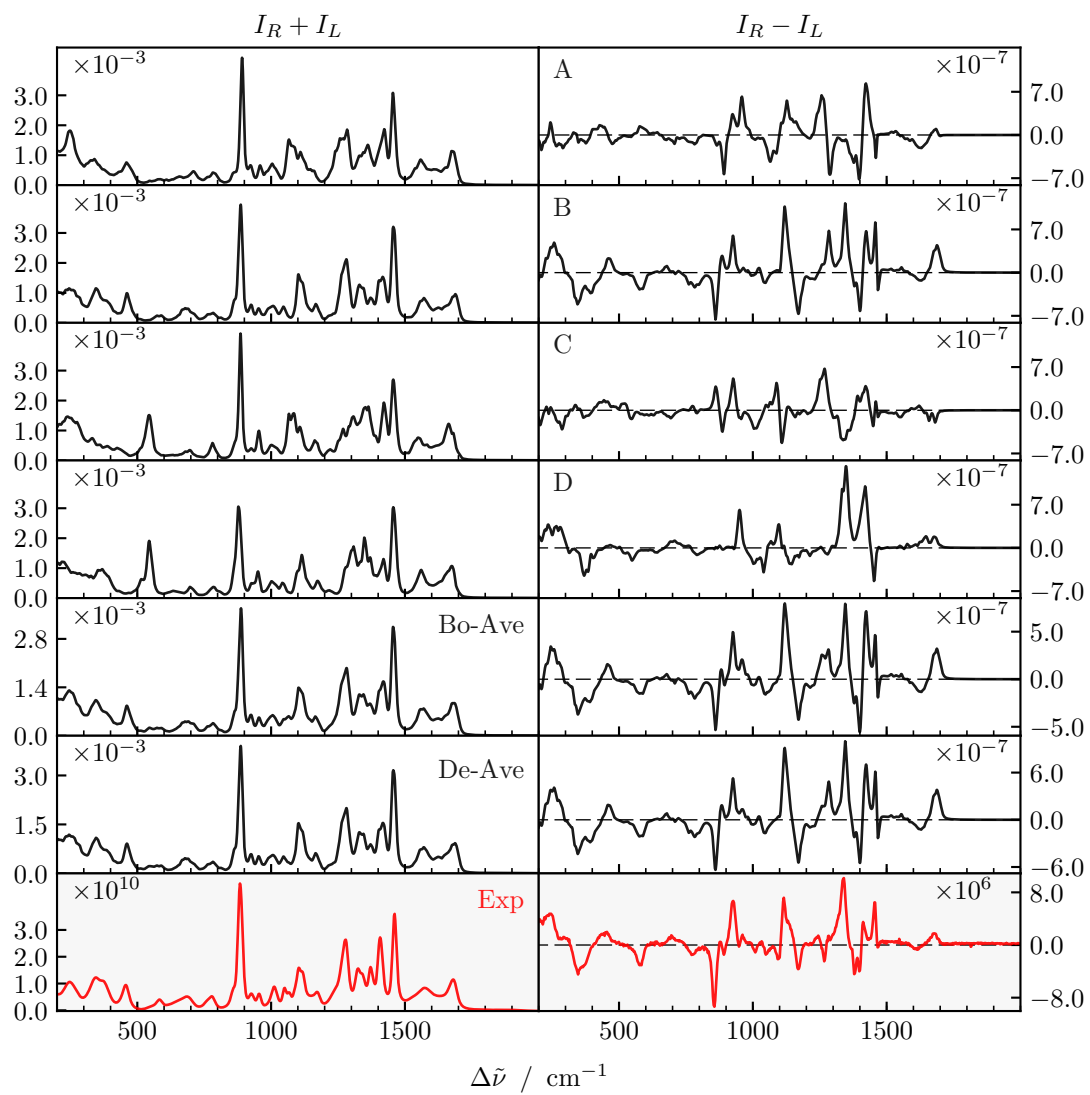Figure C.3: Protonated d8-Ala-Ala spectra.
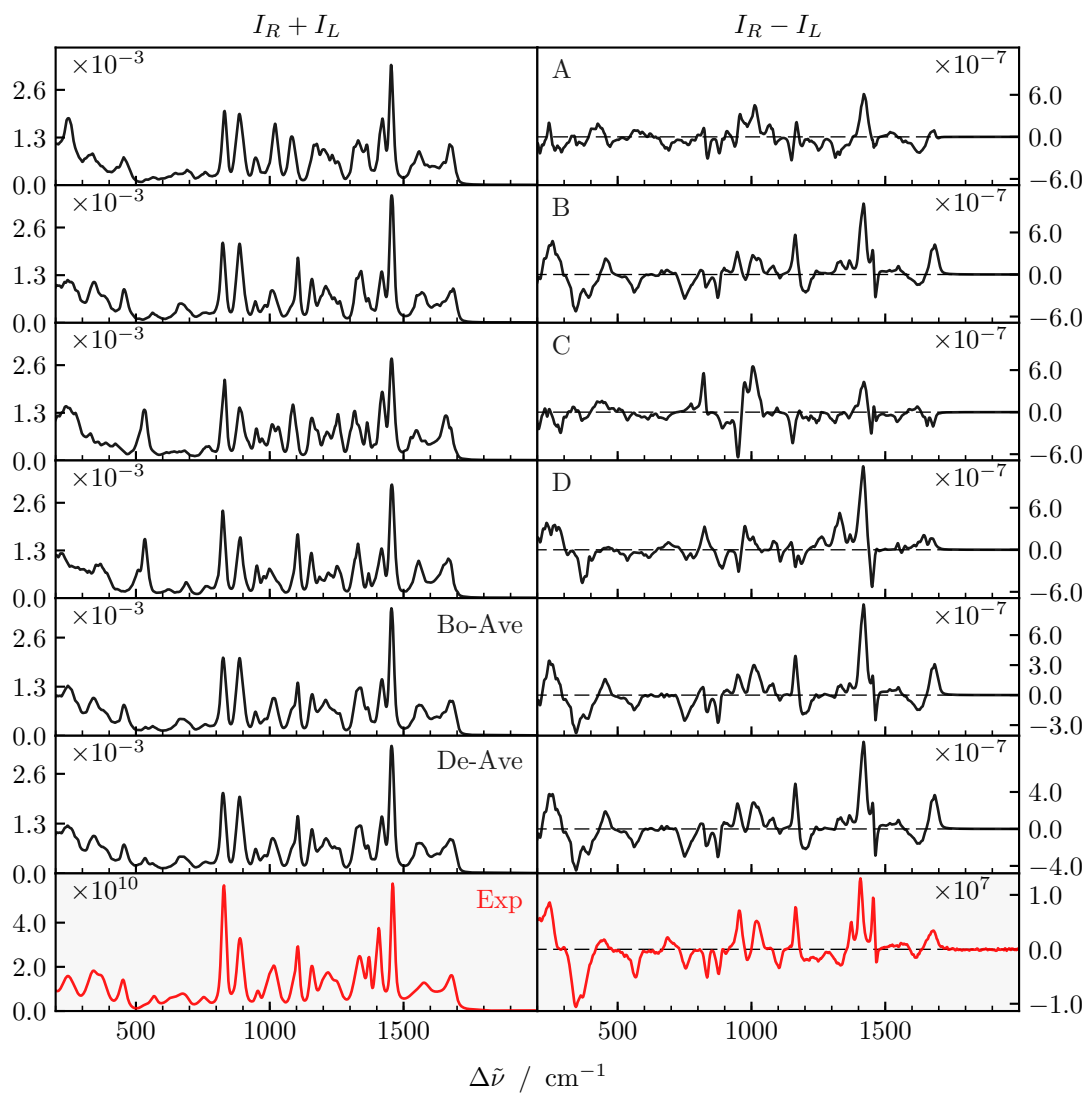
Figure C.4: Zwitterionic d0-Ala-Ala spectra.

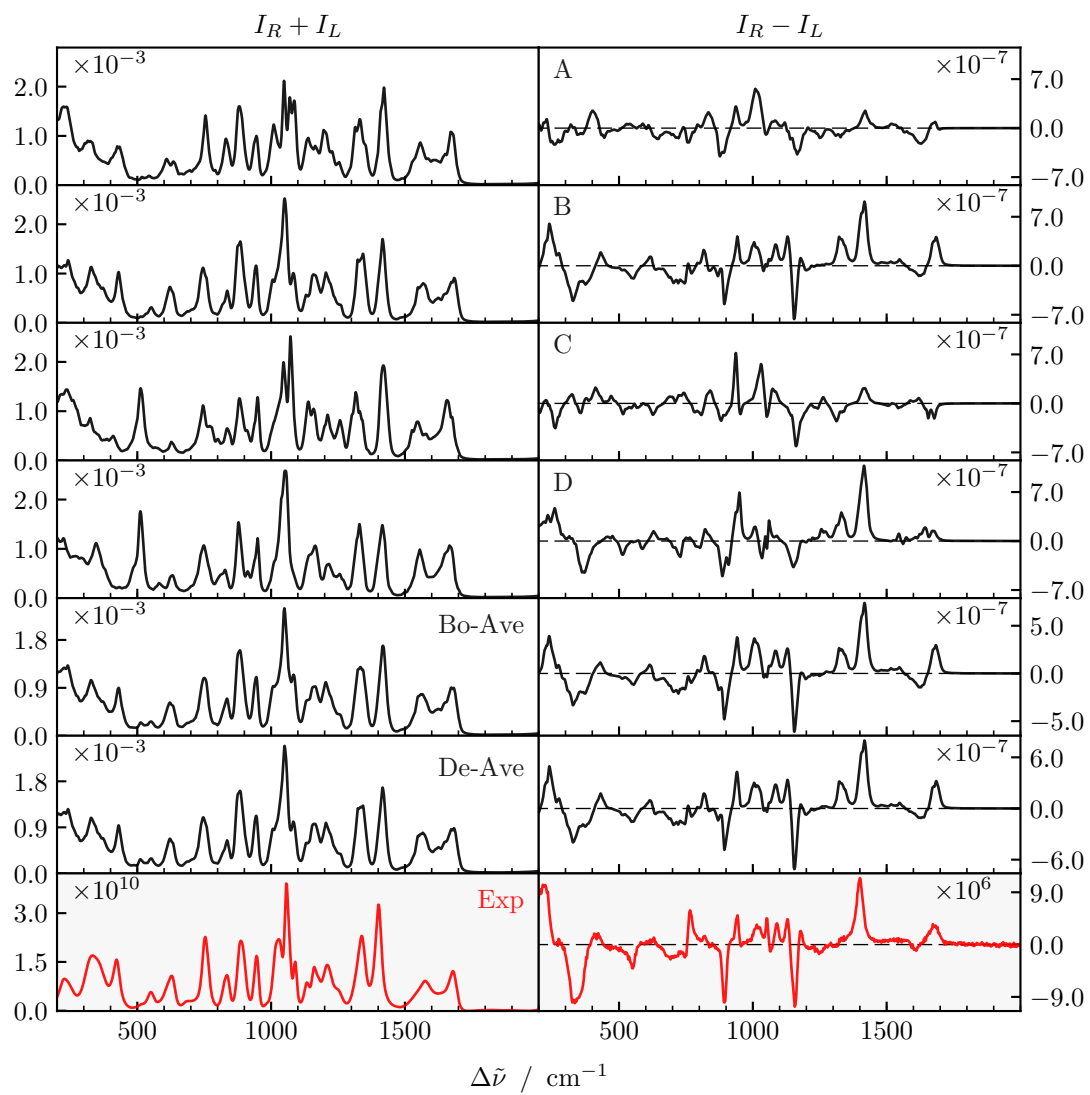Figure C.5: Zwitterionic d2-Ala-Ala spectra.
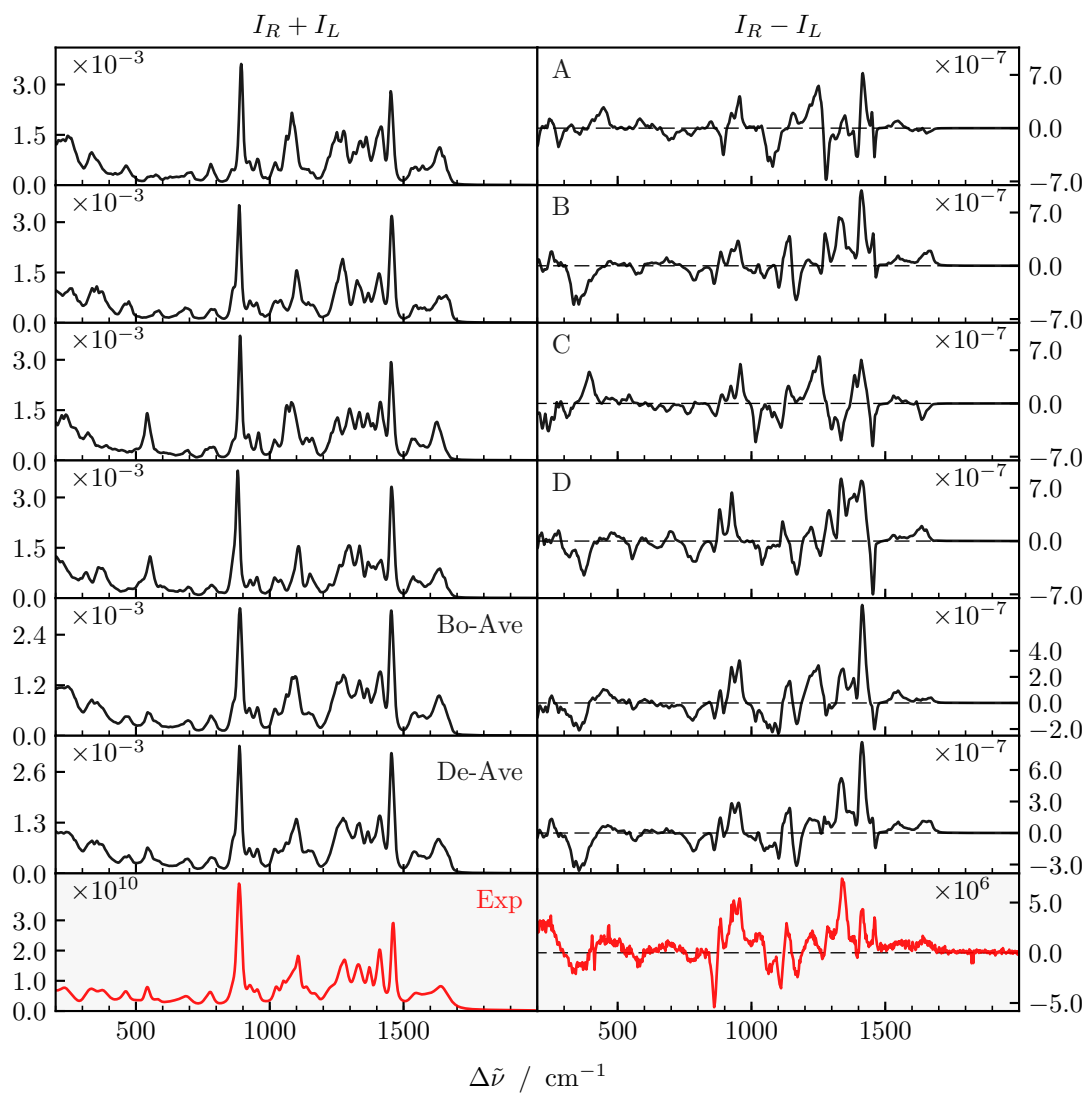
Figure C.6: Zwitterionic d8-Ala-Ala spectra.

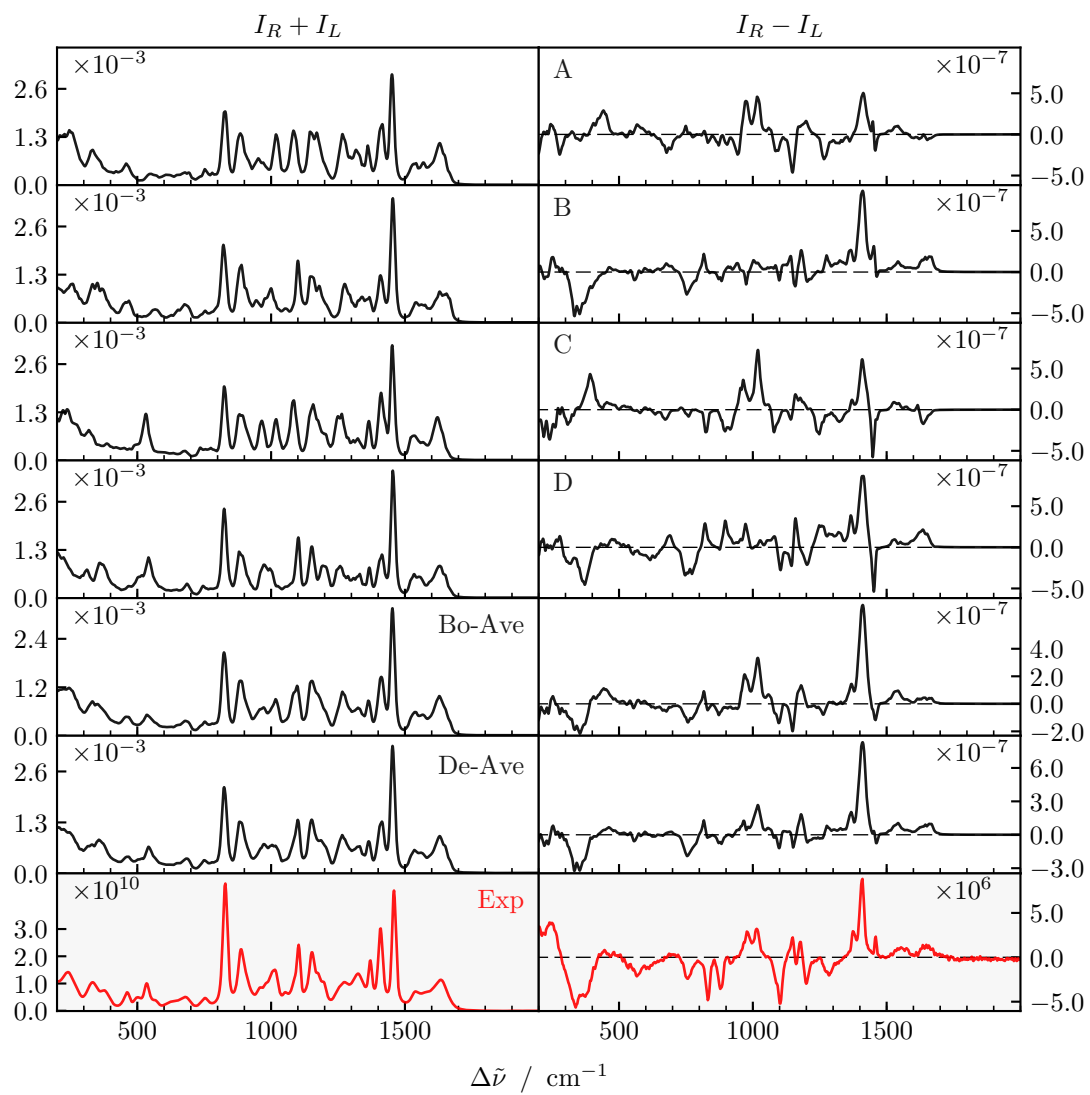Figure C.7: Deprotonated d0-Ala-Ala spectra.
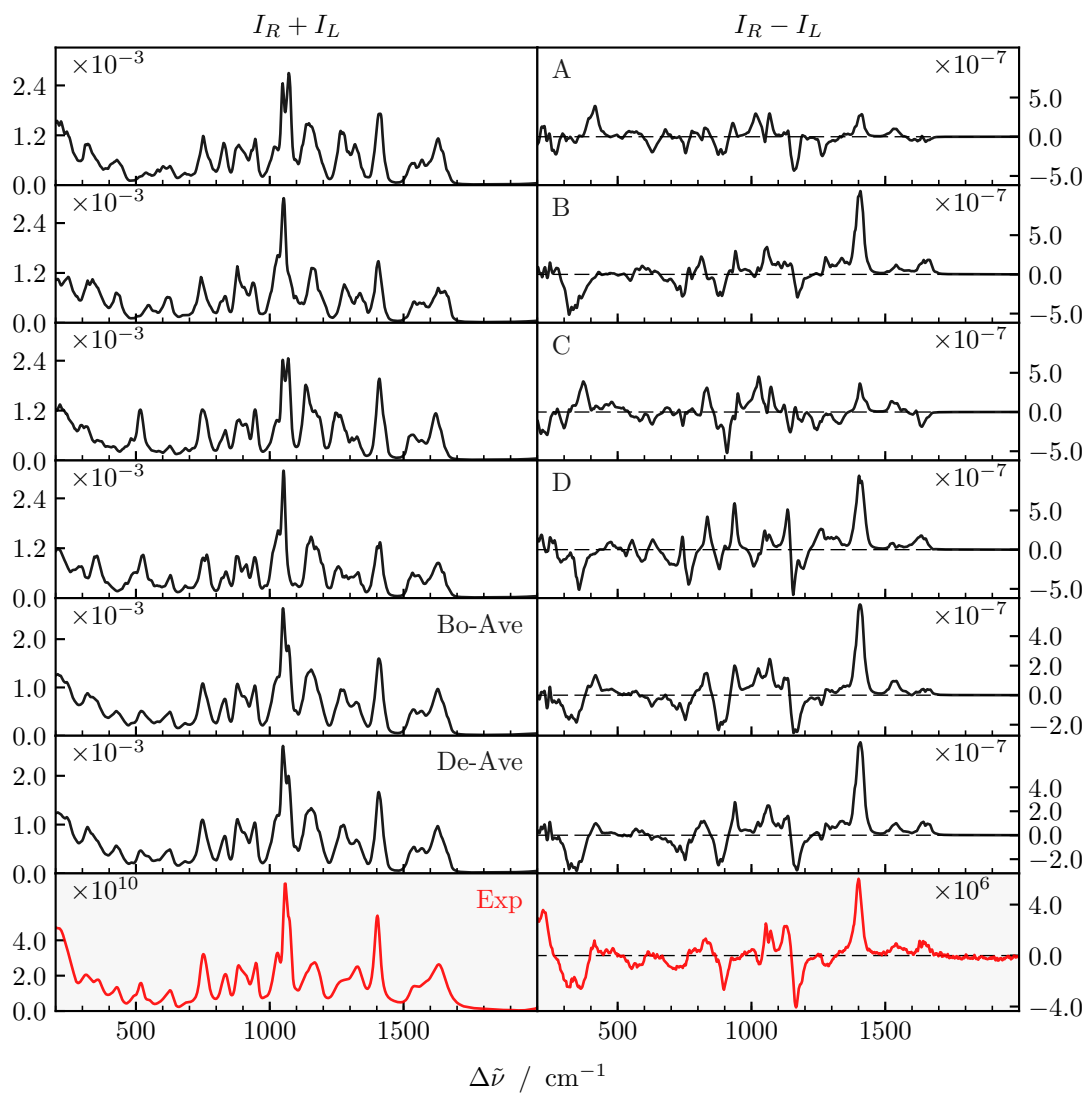
Figure C.8: Deprotonated d2-Ala-Ala spectra.

Figure C.9: Deprotonated d8-Ala-Ala spectra.

Bibliography

Ahlrichs, R., Bär, M., Häser, M., Horn, H., and Kölmel, C. (1989). Electronic structure calculations on workstation computers: The program system turbomole. *Chemical Physics Letters*, 162(3):165–169.

Aidas, K., Angeli, C., Bak, K. L., Bakken, V., Bast, R., Boman, L., Christiansen, O., Cimiraglia, R., Coriani, S., Dahle, P., et al. (2014). The Dalton quantum chemistry program system. *Wiley Interdisciplinary Reviews: Computational Molecular Science*, 4(3):269–284.

Arnaudov, L. N. and de Vries, R. (2005). Thermally induced fibrillar aggregation of hen egg white lysozyme. *Biophysical Journal*, 88(1):515–526.

Atkins, P. W. and Barron, L. D. (1969). Rayleigh scattering of polarized photons by molecules. *Molecular Physics*, 16(5):453–466.

Barron, L. D. (2004). *Molecular Light Scattering and Optical Activity, 2ⁿᵈ Edition*. Cambridge University Press.

Barron, L. D. (2015). The development of biomolecular Raman optical activity spectroscopy. *Biomedical Spectroscopy and Imaging*, 4(3):223–253.

Barron, L. D., Bogaard, M. P., and Buckingham, A. D. (1973). Raman scattering of circularly polarized light by optically active molecules. *Journal of the American Chemical Society*, 95(2):603–605.

Barron, L. D. and Buckingham, A. D. (1971). Rayleigh and Raman scattering from optically active molecules. *Molecular Physics*, 20(6):1111–1119.

Barron, L. D. and Buckingham, A. D. (1974). Simple two-group model for Rayleigh and Raman optical activity. *Journal of the American Chemical Society*, 96(15):4769–4773.

Barron, L. D. and Buckingham, A. D. (2010). Vibrational optical activity. *Chemical Physics Letters*, 492(4):199–213.

Barrow, C. J., Yasuda, A., Kenny, P. T., and Zagorski, M. G. (1992). Solution conformations and aggregational properties of synthetic amyloid β-peptides of Alzheimer's disease: analysis of circular dichroism spectra. *Journal of Molecular Biology*, 225(4):1075–1093.

Best, R. B. and Hummer, G. (2009). Optimized molecular dynamics force fields applied to the helix- coil transition of polypeptides. *The Journal of Physical Chemistry. B*, 113(26):9004.

Blanch, E. W., Hecht, L., Syme, C. D., Volpetti, V., Lomonossoff, G. P., Nielsen, K., and Barron, L. D. (2002). Molecular structures of viruses from Raman optical activity. *Journal of General Virology*, 83(10):2593–2600.

Blanch, E. W., Morozova-Roche, L. A., Cochran, D. A., Doig, A. J., Hecht, L., and Barron, L. D. (2000). Is polyproline II helix the killer conformation? A Raman optical activity study of the amyloidogenic prefibrillar intermediate of human lysozyme. *Journal of Molecular Biology*, 301(2):553–563.

Booth, D. R., Sunde, M., Bellotti, V., Robinson, C. V., et al. (1997). Instability, unfolding and aggregation of human lysozyme variants underlying amyloid fibrillogenesis. *Nature*, 385(6619):787.

Bose, P. K., Barron, L. D., and Polavarapu, P. L. (1989). Ab initio and experimental vibrational Raman optical activity in (+)-(R)-methylthiirane. *Chemical Physics Letters*, 155(4-5):423–429.

Bouř, P., Buděšínský, M., Špirko, V., Kapitán, J., Šebestík, J., and Sychrovský, V. (2005a). A complete set of NMR chemical shifts and spin-spin coupling constants for l-alanyl-l-alanine zwitterion and analysis of its conformational behavior. *Journal of the American Chemical Society*, 127(48):17079–17089.

Bouř, P., Michalík, D., and Kapitán, J. (2005b). Empirical solvent correction for multiple amide group vibrational modes. *The Journal of Chemical Physics*, 122(14):144501.

Bouř, P. and Keiderling, T. A. (2002). Partial optimization of molecular geometry in normal coordinates and use as a tool for simulation of vibrational spectra. *The Journal of Chemical Physics*, 117(9):4126–4132.

Boyd, R. W. (2008). *Nonlinear Optics, Third Edition*. Elsevier, Inc.

Buděšínský, M., Daněček, P., Bednárová, L., Kapitán, J., Baumruk, V., and Bouř, P. (2008). Comparison of quantitative conformer analyses by nuclear magnetic resonance and Raman optical activity spectra for model dipeptides. *The Journal of Physical Chemistry A*, 112(37):8633–8640.

Cances, E., Mennucci, B., and Tomasi, J. (1997). A new integral equation formalism for the polarizable continuum model: Theoretical background and applications to isotropic and anisotropic dielectrics. *The Journal of Chemical Physics*, 107(8):3032–3041.

Case, D. A., Cheatham, T. E., Darden, T., Gohlke, H., Luo, R., Merz, K. M., Onufriev, A., Simmerling, C., Wang, B., and Woods, R. J. (2005). The Amber biomolecular simulation programs. *Journal of Computational Chemistry*, 26(16):1668–1688.

Choi, J.-H. and Cho, M. (2009). Amide I Raman optical activity of polypeptides: Fragment approximation. *The Journal of Chemical Physics*, 130(1):014503.

Come, J. H., Fraser, P. E., and Lansbury, P. T. (1993). A kinetic model for amyloid formation in the prion diseases: importance of seeding. *Proceedings of the National Academy of Sciences*, 90(13):5959–5963.

Cornell, W. D., Cieplak, P., Bayly, C. I., Gould, I. R., Merz, K. M., Ferguson, D. M., Spellmeyer, D. C., Fox, T., Caldwell, J. W., and Kollman, P. A. (1996).

A second generation force field for the simulation of proteins, nucleic acids, and organic molecules. *Journal of the American Chemical Society*, 118(9):2309–2309.

Cortez, M. H., Brinkmann, N. R., Polik, W. F., Taylor, P. R., Bomble, Y. J., and Stanton, J. F. (2007). Factors contributing to the accuracy of harmonic force field calculations for water. *Journal of Chemical Theory and Computation*, 3(4):1267–1274.

Cossi, M., Rega, N., Scalmani, G., and Barone, V. (2003). Energies, structures, and electronic properties of molecules in solution with the C-PCM solvation model. *Journal of Computational Chemistry*, 24(6):669–681.

Creighton, T. E. (1993). *Proteins: structures and molecular properties*. Macmillan.

Daněček, P., Kapitán, J., Baumruk, V., Bednárová, L., Kopecký Jr, V., and Bouř, P. (2007). Anharmonic effects in IR, Raman, and Raman optical activity spectra of alanine and proline zwitterions. *The Journal of Chemical Physics*, 126(22):224513.

Duan, Y., Wu, C., Chowdhury, S., Lee, M. C., Xiong, G., Zhang, W., Yang, R., Cieplak, P., Luo, R., Lee, T., et al. (2003). A point-charge force field for molecular mechanics simulations of proteins based on condensed-phase quantum mechanical calculations. *Journal of Computational Chemistry*, 24(16):1999–2012.

Dukor, R. K. and Keiderling, T. A. (1991). Reassessment of the random coil conformation: vibrational CD study of proline oligopeptides and related polypeptides. *Biopolymers*, 31(14):1747–1761.

Eliel, E. L. and Wilen, S. H. (2008). *Stereochemistry of Organic Compounds*. John Wiley & Sons.

Foloppe, N. and MacKerell Jr, A. D. (2000). All-atom empirical force field for nucleic acids: I. Parameter optimization based on small molecule and condensed phase macromolecular target data. *Journal of Computational Chemistry*, 21(2):86–104.

Frisch, M. J., Trucks, G. W., Schlegel, H. B., Scuseria, G. E., Robb, M. A., Cheeseman, J. R., Scalmani, G., Barone, V., Mennucci, B., Petersson, G. A., et al. (2013). Gaussian 09, Revision D. 01.

Haesler, J., Schindelholz, I., Riguet, E., Bochet, C. G., and Hug, W. (2007). Absolute configuration of chirally deuterated neopentane. *Nature*, 446(7135):526–529.

Hecht, L., Barron, L. D., and Hug, W. (1989). Vibrational Raman optical activity in backscattering. *Chemical Physics Letters*, 158(5):341–344.

Herrmann, C., Ruud, K., and Reiher, M. (2006). Can Raman optical activity separate axial from local chirality? A theoretical study of helical deca-alanine. *ChemPhysChem*, 7(10):2189–2196.

Hobro, A. J., Rouhi, M., Conn, G. L., and Blanch, E. W. (2008). Raman and Raman optical activity (ROA) analysis of RNA structural motifs. *Vibrational Spectroscopy*, 48(1):37–43.

Hopmann, K. H., Ruud, K., Pecul, M., Kudelski, A., Dračínský, M., and Bouř, P. (2011). Explicit versus implicit solvent modeling of Raman optical activity spectra. *The Journal of Physical Chemistry B*, 115(14):4128–4137.

Horný, L., Mach, P., Masarik, J., Hubač, I., and Wilson, S. (2013). Theoretical study of the HeN_2^{2+} dication. *Molecular Physics*, 111(24):3801–3807.

Hudecová, J., Hopmann, K. H., and Bour, P. (2011). Correction of vibrational broadening in molecular dynamics clusters with the normal mode optimization method. *The Journal of Physical Chemistry B*, 116(1):336–342.

Hug, W. (2001). Visualizing Raman and Raman optical activity generation in polyatomic molecules. *Chemical Physics*, 264(1):53–69.

Hug, W. (2003). Virtual enantiomers as the solution of optical activity's deterministic offset problem. *Applied spectroscopy*, 57(1):1–13.

Hug, W. (2012). Measurement of Raman optical activity. In Berova, N., Polavarapu, P. L., Nakanishi, K., and Woody, R. W., editors, *Comprehensive Chiroptical Spectroscopy: Instrumentation, Methodologies, and Theoretical Simulations. Vol. 1*, chapter 6, pages 147–177. John Wiley & Sons, Inc.

Hug, W. and Hangartner, G. (1999). A novel high-throughput Raman spectrometer for polarization difference measurements. *Journal of Raman Spectroscopy*, 30(9):841–852.

Hug, W., Kint, S., Bailey, G. F., and Scherer, J. R. (1975). Raman circular intensity differential spectroscopy. spectra of (–)-. alpha.-pinene and (+)-. alpha.-phenylethylamine. *Journal of the American Chemical Society*, 97(19):5589–5590.

Jalkanen, K. J., Nieminen, R., Knapp-Mohammady, M., and Suhai, S. (2003). Vibrational analysis of various isotopomers of L-Alanyl-L-Alanine in aqueous solution: Vibrational absorption, vibrational circular dichroism, Raman, and Raman optical activity spectra. *International Journal of Quantum Chemistry*, 92(2):239–259.

Jovan Jose, K. and Raghavachari, K. (2016). Raman optical activity spectra for large molecules through molecules-in-molecules fragment-based approach. *Journal of Chemical Theory and Computation*, 12(2):585–594.

Jungwirth, J. (2014). *Explicitly Correlated Multireference Coupled-Cluster Study of Molecules and Cations with Diradical Character*. Bachelor's thesis, Charles University, Prague, Czechia.

Kaminský, J., Kapitán, J., Baumruk, V., Bednárová, L., and Bouř, P. (2009). Interpretation of Raman and Raman optical activity spectra of a flexible sugar derivative, the gluconic acid anion. *The Journal of Physical Chemistry A*, 113(15):3594–3601.

Kastler, A. (1930). *Comptes Rendus*, 191:565.

Kessler, J., Kapitán, J., and Bouř, P. (2015). First-principles predictions of vibrational Raman optical activity of globular proteins. *The Journal of Physical Chemistry Letters*, 6(16):3314–3319.

Klamt, A. (1998). COSMO and COSMO-RS. In Dolg, M., Schleyer, P. v. R., Allinger, N., Clark, T., Gasteiger, J., Kollman, P., Schaefer III, H., and Schreiner, P., editors, *The Encyclopedia of Computational Chemistry*, pages 604 – 615. Wiley, Chichester.

Knapp-Mohammady, M., Jalkanen, K. J., Nardi, F., Wade, R. C., and Suhai, S. (1999). L-Alanyl-L-alanine in the zwitterionic state: structures determined in the presence of explicit water molecules and with continuum models using density functional theory. *Chemical Physics*, 240(1):63–77.

Koch, W. and Holthausen, M. C. (2015). *A Chemist's Guide to Density Functional Theory*. John Wiley & Sons.

Koolman, J., Röhm, K.-H., Wirth, J., and Robertson, M. (2005). *Color Atlas of Biochemistry, 2nd Edition*. Thieme Stuttgart.

Kumar, S., Rosenberg, J. M., Bouzida, D., Swendsen, R. H., and Kollman, P. A. (1992). The weighted histogram analysis method for free-energy calculations on biomolecules. I. The method. *Journal of Computational Chemistry*, 13(8):1011–1021.

LeVine, H. (1995). Thioflavine T interaction with amyloid β-sheet structures. *Amyloid*, 2(1):1–6.

Li, H. and Nafie, L. A. (2012). Simultaneous acquisition of all four forms of circular polarization Raman optical activity: results for α-pinene and lysozyme. *Journal of Raman Spectroscopy*, 43(1):89–94.

Luber, S. and Reiher, M. (2009). Theoretical Raman optical activity study of the β domain of rat metallothionein. *The Journal of Physical Chemistry B*, 114(2):1057–1063.

Ma, S., Cao, X., Mak, M., Sadik, A., Walkner, C., Freedman, T. B., Lednev, I. K., Dukor, R. K., and Nafie, L. A. (2007). Vibrational circular dichroism shows unusual sensitivity to protein fibril formation and development in solution. *Journal of the American Chemical Society*, 129(41):12364–12365.

Makin, O. S., Sikorski, P., and Serpell, L. C. (2006). Diffraction to study protein and peptide assemblies. *Current Opinion in Chemical Biology*, 10(5):417–422.

Missmahl, H.-P. and Hartwig, M. (1953). Polarisationsoptische Untersuchungen an der Amyloidsubstanz. *Virchows Archiv*, 324(4):489–508.

Nafie, L. A. (2008). Theory of Raman scattering and Raman optical activity: near resonance theory and levels of approximation. *Theoretical Chemistry Accounts: Theory, Computation, and Modeling (Theoretica Chimica Acta)*, 119(1):39–55.

Nafie, L. A. (2011). *Vibrational Optical Activity: Principles and Applications.* John Wiley & Sons.

Oboodi, M. R., Alva, C., and Diem, M. (1984). Solution-phase Raman studies of alanyl dipeptides and various isotopomers: a reevaluation of the amide iii vibrational assignment. *The Journal of Physical Chemistry*, 88(3):501–505.

Parchaňský, V., Kapitán, J., and Bouř, P. (2014). Inspecting chiral molecules by Raman optical activity spectroscopy. *RSC Advances*, 4(100):57125–57136.

Parchaňský, V., Kapitán, J., Kaminský, J., Šebestík, J., and Bouř, P. (2013). Ramachandran plot for alanine dipeptide as determined from Raman optical activity. *The Journal of Physical Chemistry Letters*, 4(16):2763–2768.

Pecul, M. and Rizzo, A. (2003). Raman optical activity spectra: basis set and electron correlation effects. *Molecular Physics*, 101(13):2073–2081.

Polavarapu, P. L. (1982). Atomic Raman tensors and intensity sum rule. *Journal of Molecular Spectroscopy*, 93(2):450–452.

Polavarapu, P. L. and Covington, C. L. (2014). Comparison of experimental and calculated chiroptical spectra for chiral molecular structure determination. *Chirality*, 26(9):539–552.

Prampolini, G., Livotto, P. R., and Cacelli, I. (2015). Accuracy of quantum mechanically derived force-fields parameterized from dispersion-corrected DFT data: The benzene dimer as a prototype for aromatic interactions. *Journal of Chemical Theory and Computation*, 11(11):5182–5196.

Rambaran, R. N. and Serpell, L. C. (2008). Amyloid fibrils. *Prion*, 2(3):112–117.

Ruud, K. (2012). *Ab initio* methods for vibrational circular dichroism and Raman optical activity. In Berova, N., Polavarapu, P. L., Nakanishi, K., and Woody, R. W., editors, *Comprehensive Chiroptical Spectroscopy: Instrumentation, Methodologies, and Theoretical Simulations. Vol. 1*, chapter 24, pages 699–727. John Wiley & Sons, Inc.

Ruud, K., Helgaker, T., and Bouř, P. (2002). Gauge-origin independent density-functional theory calculations of vibrational Raman optical activity. *The Journal of Physical Chemistry A*, 106(32):7448–7455.

Ruud, K. and Thorvaldsen, A. J. (2009). Theoretical approaches to the calculation of raman optical activity spectra. *Chirality*, 21(1E).

Šebestík, J. and Bouř, P. (2014). Observation of paramagnetic Raman optical activity of nitrogen dioxide. *Angewandte Chemie*, 126(35):9390–9393.

Seco, J. M., Quinoá, E., and Riguera, R. (2004). The assignment of absolute configuration by NMR. *Chemical Reviews*, 104(1):17–118.

Selkoe, D. J. (2003). Folding proteins in fatal ways. *Nature*, 426(6968):900–904.

Sellers, H., Klimkowski, V., and Schäfer, L. (1978). Normal coordinate ab initio force relaxation. *Chemical Physics Letters*, 58(4):541–544.

Sipe, J. D. and Cohen, A. S. (2000). Review: History of the amyloid fibril. *Journal of Structural Biology*, 130(2-3):88–98.

Sreerama, N. and Woody, R. (2000). Circular dichroism of peptides and proteins. *Circular dichroism: Principles and applications*, 2:601–620.

Stathopulos, P. B., Scholz, G. A., Hwang, Y.-M., Rumfeldt, J. A., Lepock, J. R., and Meiering, E. M. (2004). Sonication of proteins causes formation of aggregates that resemble amyloid. *Protein Science*, 13(11):3017–3027.

Sychrovský, V., Budešínský, M., Benda, L., Špirko, V., Vokáčová, Z., Šebestík, J., and Bouř (2008). Dependence of the L-alanyl-L-alanine conformation on molecular charge determined from ab initio computations and NMR spectra. *The Journal of Physical Chemistry B*, 112(6):1796–1805.

Szabo, A. and Ostlund, N. S. (1996). *Modern Quantum Chemistry: Introduction to Advanced Electronic Structure Theory*. Dover Publications.

Šebek, J., Gyurcsik, B., Šebestík, J., Kejík, Z., Bednárová, L., and Bouř, P. (2007). Interpretation of synchrotron radiation circular dichroism spectra of anionic, cationic, and zwitterionic dialanine forms. *environment*, 13(22):24–31.

Šebek, J., Kapitán, J., Šebestík, J., Baumruk, V., and Bouř, P. (2009). L-alanyl-L-alanine conformational changes induced by pH as monitored by the Raman optical activity spectra. *The Journal of Physical Chemistry A*, 113(27):7760–7768.

Wang, J., Cieplak, P., and Kollman, P. A. (2000). How well does a restrained electrostatic potential (RESP) model perform in calculating conformational energies of organic and biological molecules? *Journal of Computational Chemistry*, 21(12):1049–1074.

Weir, A. F., Lowrey, A. H., and Williams, R. W. (2001). Scaled quantum mechanical force field for alanyl–alanine peptide in solution. *Biopolymers*, 58(6):577–591.

Wetter, L. R. and Deutsch, H. F. (1951). Immunological studies on egg white proteins IV. Immunochemical and physical studies of lysozyme. *Journal of Biological Chemistry*, 192(1):237–242.

Yaffe, N. R., Almond, A., and Blanch, E. W. (2010). A new route to carbohydrate secondary and tertiary structure using Raman spectroscopy and Raman optical activity. *Journal of the American Chemical Society*, 132(31):10654–10655.

Yamamoto, S., Furukawa, T., Bouř, P., and Ozaki, Y. (2014). Solvated states of poly-l-alanine α-helix explored by Raman optical activity. *The Journal of Physical Chemistry A*, 118(20):3655–3662.

Yamamoto, S., Li, X., Ruud, K., and Bouř, P. (2012). Transferability of various molecular property tensors in vibrational spectroscopy. *Journal of Chemical Theory and Computation*, 8(3):977–985.

Yamamoto, S. and Watarai, H. (2010). Incident circularly polarized Raman optical activity spectrometer based on circularity conversion method. *Journal of Raman Spectroscopy*, 41(12):1664–1669.

Yamamoto, S. and Watarai, H. (2012). Raman optical activity study on insulin amyloid-and prefibril intermediate. *Chirality*, 24(2):97.

Yu, G.-S., Che, D., Freedman, T. B., and Nafie, L. A. (1995). Raman optical activity of simple alanyl peptides: Backscattering in-phase dual circular polarization measurements in aqueous solution. *Biospectroscopy*, 1(2):113–123.

Yu, G.-S. and Nafie, L. A. (1994). Isolation of preresonance and out-of-phase dual circular polarization Raman optical activity. *Chemical Physics Letters*, 222(4):403–410.